ARMY RESEARCH LABORATORY

Synthetic Aperture Radar Images of a Simple Room Based on Computer Models

by Traian Dogaru, Calvin Le, and Lam Nguyen

ARL-TR-5193 **May 2010**

NOTICES

Disclaimers

The findings in this report are not to be construed as an official Department of the Army position unless so designated by other authorized documents.

Citation of manufacturer's or trade names does not constitute an official endorsement or approval of the use thereof.

Destroy this report when it is no longer needed. Do not return it to the originator.

Army Research Laboratory
Adelphi, MD 20783-1197

ARL-TR-5193 **May 2010**

Synthetic Aperture Radar Images of a Simple Room Based on Computer Models

Traian Dogaru, Calvin Le, and Lam Nguyen
Sensors and Electron Devices Directorate, ARL

REPORT DOCUMENTATION PAGE

Form Approved
OMB No. 0704-0188

1. REPORT DATE *(DD-MM-YYYY)*	2. REPORT TYPE	3. DATES COVERED (From - To)
May 2010	Final	2007 to 2010

4. TITLE AND SUBTITLE
Synthetic Aperture Radar Images of a Simple Room Based on Computer Models

5a. CONTRACT NUMBER

5b. GRANT NUMBER

5c. PROGRAM ELEMENT NUMBER

6. AUTHOR(S)
Traian Dogaru, Calvin Le, and Lam Nguyen

5d. PROJECT NUMBER

5e. TASK NUMBER

5f. WORK UNIT NUMBER

7. PERFORMING ORGANIZATION NAME(S) AND ADDRESS(ES)
U.S. Army Research Laboratory
ATTN: RDRL-SER-U
2800 Powder Mill Road
Adelphi, MD 20783-1197

8. PERFORMING ORGANIZATION REPORT NUMBER
ARL-TR-5193

9. SPONSORING/MONITORING AGENCY NAME(S) AND ADDRESS(ES)

10. SPONSOR/MONITOR'S ACRONYM(S)

11. SPONSOR/MONITOR'S REPORT NUMBER(S)

12. DISTRIBUTION/AVAILABILITY STATEMENT
Approved for public release; distribution unlimited.

13. SUPPLEMENTARY NOTES

14. ABSTRACT
This report investigates the application of synthetic aperture radar (SAR) imaging techniques to sensing through the wall (STTW) scenarios based on radar data obtained through computer simulation of electromagnetic (EM) scattering problems using either the Finite Difference Time Domain (FDTD) method or Xpatch. We analyze the radar phenomenology for simple through-the-wall imaging scenarios and offer guidelines for a performance prediction and radar parameter trade-off. Our simulations show that, for these configurations, SAR techniques clearly resolve human targets when the construction material is brick, but do not achieve the same performance for concrete or cinder block walls. We demonstrate that using the cross-polarization radar mode can result in enhanced target-to-clutter ratios. By comparing the images obtained through the FDTD and Xpatch simulations, we show that both modeling methods achieve reasonable accuracy for this type of application. We also discuss two imaging formation techniques (spotlight and strip-map) and emphasize the differences in the resulting images. The existence of ghost images in a STTW scenario is explained by analyzing multipath propagation effects inside a room.

15. SUBJECT TERMS
Radar, sensing through the wall

16. SECURITY CLASSIFICATION OF:			17. LIMITATION OF ABSTRACT	18. NUMBER OF PAGES	19a. NAME OF RESPONSIBLE PERSON
a. REPORT	b. ABSTRACT	c. THIS PAGE			Traian Dogaru
Unclassified	Unclassified	Unclassified	UU	62	19b. TELEPHONE NUMBER (*Include area code*) (301) 394-1482

Standard Form 298 (Rev. 8/98)
Prescribed by ANSI Std. Z39.18

Contents

List of Figures

Acknowledgments

This study was partially funded by the Communications-Electronics Research Development and Engineering Center (CERDEC), Intelligence and Information Warfare Directorate (I2WD) at Ft. Monmouth, NJ.

INTENTIONALLY LEFT BLANK.

1. Introduction

For the last several years, the U.S. Army Research Laboratory (ARL) has been involved in the Army's efforts to develop sensing through the wall (STTW) radar technology. Our contribution has mostly consisted of radar system modeling and analysis in support of various Army STTW programs. The emphasis has been on understanding the radar scattering phenomenology, developing signal processing algorithms, and studying design parameter trade-offs, with the purpose of creating guidelines for optimized radar system performance. Our previous research has been reported in several publications and includes analysis of the stationary human radar signature (*1–3*); use of advanced computational electromagnetic (CEM) codes for modeling radar scattering in complex STTW scenarios (*4*); high-resolution synthetic aperture radar (SAR) techniques based on multi-static sensor arrays (*5*); analysis of a moving human Doppler signature (*6*); and investigation of moving target indicator (MTI) techniques as applied to a STTW environment (*7*). Additionally, the Radio Frequency (RF) Signal Processing and Modeling Branch at ARL has performed field measurements using the in-house-developed Synchronous Impulse Reconstruction (SIRE) radar, demonstrating its capabilities in imaging complex buildings and detecting behind-the-wall targets (*8, 9*).

The investigation reported here continues our efforts in STTW radar performance modeling and prediction through computer simulations by looking at issues related to the SAR imaging of STTW scenarios. Radar imaging can be used in through-the-wall sensing applications for either building mapping or behind-the-wall target detection (human targets, in particular, but weapon caches may be of interest as well). Specific performance requirements apply to each of these cases. While we analyze detailed technical aspects of both the electromagnetic (EM) modeling and the image formation processes, the ultimate goal is to suggest solutions for improved radar system performance in these applications. The results of our models are typically much cleaner than real radar data and, in that sense, they represent the "best case scenario" for radar performance. Nevertheless, being able to separate out the artifacts generated by real radar system electronics and signal processing allows us to focus our investigation on fundamental EM propagation and scattering effects, as well as image formation algorithms. While some of our simulated STTW radar imaging scenarios may be somewhat contrived, they still convey some important phenomenological insight into this complex technology application.

Computer modeling of the EM propagation and scattering involving large targets, such as rooms and buildings, require both accurate CEM solvers and powerful computer hardware systems. For the purpose of creating ultra-wideband (UWB) SAR images, we need to perform these simulations over a large number of frequencies and aspect angles. In this study, we employ the Finite Difference Time Domain (FDTD) and Xpatch computer codes. We discuss the efficiency, accuracy and domain of applicability of these methods in modeling radar scattering in a STTW

environment. We also compare two different SAR imaging techniques, namely, the backprojection algorithm and the polar format algorithm (*10–12*). Although the former is a more accurate image formation algorithm, it is also more computationally intensive. We demonstrate that, under certain assumptions, the accuracy of the polar format algorithm in creating SAR images for the scenarios of interest is satisfactory.

The issue of near-field versus far-field geometry for through-the-wall imaging radar is also explored in this report. Given the large target dimensions and relatively small standoff radar ranges specific to most STTW scenarios, the EM scattering problem is better characterized by near-field geometry. However, calculating the radar return in the near-field case is very challenging from a computational standpoint. Therefore, most of our SAR image examples assume far-field geometry. We attempt to validate this approach by comparing the images based on the near-field to the far-field responses of the same scene.

In this report, we study the SAR images of a simple four-wall room, containing one or two targets. We investigate several construction materials and techniques, as well as various radar parameters (frequency of operation, bandwidth, aspect angle, aperture size, and polarization). We demonstrate the advantages of operating the radar in cross-polarization mode for applications that require emphasizing human targets while rejecting the clutter produced by walls and other objects. One particular issue specific to imaging localized targets placed in a room is the presence of "ghost" images. Our analysis shows that this is the effect of multipath propagation and predicts the location of the ghost images relative to the actual target position.

This report is organized as follows. In section 2, we discuss the algorithms used in modeling the EM scattering problem, as well as the image formation process. In section 3, we show the numerical results obtained for the entire variety of scenarios indicated in the previous paragraphs. Section 4 outlines ours conclusions. The appendix presents an analysis of the multipath issue for target imaging in a room.

2. Simulation Methodology

2.1 Electromagnetic Modeling

In order to create the SAR images of targets, we must first obtain the radar signature of those targets for various antenna positions or angles. In this study, we obtain this signature through computer simulations. For this purpose, we use two CEM codes: AFDTD (*13*), which is based on the FDTD technique, and Xpatch, which is a combination of ray tracing and physical optics (PO) approaches. Some basic features of these codes were mentioned in Dogaru and Le (*4*), while more comprehensive descriptions of FDTD and PO can be found in classic references (*14, 15*). It is important to mention that AFDTD was developed at ARL and implements an "exact" CEM method, whereas Xpatch was developed by Science Applications International Corporation

(SAIC) under a grant from the U.S. Air Force and implements an "approximate" EM solver. AFDTD is a very computationally intensive code both in terms of central processing unit (CPU) time and memory, which makes Xpatch an attractive approach for rapid modeling of very complex scenarios. However, before we can apply Xpatch to the specific problem of through-the-wall radar imaging, we need to validate the method against an exact solution (such as that provided by AFDTD). Although most of the results presented in this work are based on AFDTD simulations, some results in section 3 are produced by Xpatch, including a validation of this method in section 3.3.

We should mention that the general FDTD algorithm is not completely error free and needs to be carefully applied to specific modeling scenarios. The main source of errors is the numerical dispersion (*14*), which imposes upper limits on the FDTD cell size in order to keep the propagation errors under control. Previously, we made an assessment of these errors for scenarios identical to the ones investigated in this report (*4*). Another modeling issue, this time specific to the AFDTD code, is the dielectric loss model for the wall materials (as discussed in section 2.3). However, since the radar waves propagate for relatively short distances within these materials, the errors introduced are not significant, as demonstrated by the good match with Xpatch (which treats this effect correctly).

Another important aspect that needs to be mentioned here is the distinction between far-field and near-field modeling of the SAR data collection geometry. The generic FDTD technique can (in principle) produce both near-field and far-field radar signatures and has been used in near-field room imaging by other researchers (*16*). However, this approach presents issues in simulating a realistic STTW scenario, both in terms of standoff distance from radar to target and implementing actual antenna patterns. The AFDTD code is designed to provide only far-field radar modeling, using plane-wave excitation. On the other hand, Xpatch can provide both far- and near-field radar signatures. Whereas the Xpatch far-field simulations use plane-wave excitation (or, more exactly, shoots bundles of rays with the same direction), similarly to AFDTD, the near-field modeling involves shooting bundles of rays in different directions, that closely follow a realistic antenna pattern. The received signal is computed using the PO approach, with the antenna pattern modulating the fields scattered by the target in various directions (typically the transmitting and receiving antennas are considered to have the same pattern). More details on this type of modeling are provided in section 3.5. The implications of the far- versus near-field geometry for the SAR imaging process will become evident in the next section.

2.2 SAR Imaging Techniques

With the significant advances made over the last two decades in both radar electronics and computational power, the SAR has become a major technology for remote sensing applications, allowing the collection of high-resolution imagery in environments where optical or infrared sensors do not perform well. A description of this technology and the algorithms involved in

image formation can be found in numerous textbooks (*10–12*). In this study, we simulate SAR scenarios that create two-dimensional (2-D) images (in the *x-y*, or horizontal, plane) of a room. Throughout this report we assume monostatic radar operation (meaning that the transmitter and receiver are collocated). We look at two different SAR imaging techniques: strip-map and spotlight (*10*). Current ground-based STTW imaging radar systems use the strip-map geometry (*8, 17, 18*). The basic scenario is described in figure 1a, where the radar is mounted on a vehicle looking sideways with respect to the driving direction—which in most cases is parallel to one side of the building. Although the spotlight configuration (described in figure 1b) is not representative for current STTW SAR technology, it is more convenient to model from a computational complexity standpoint, so most of our numerical examples employ the latter technique. We analyze the differences between the two basic configurations in section 3.5.

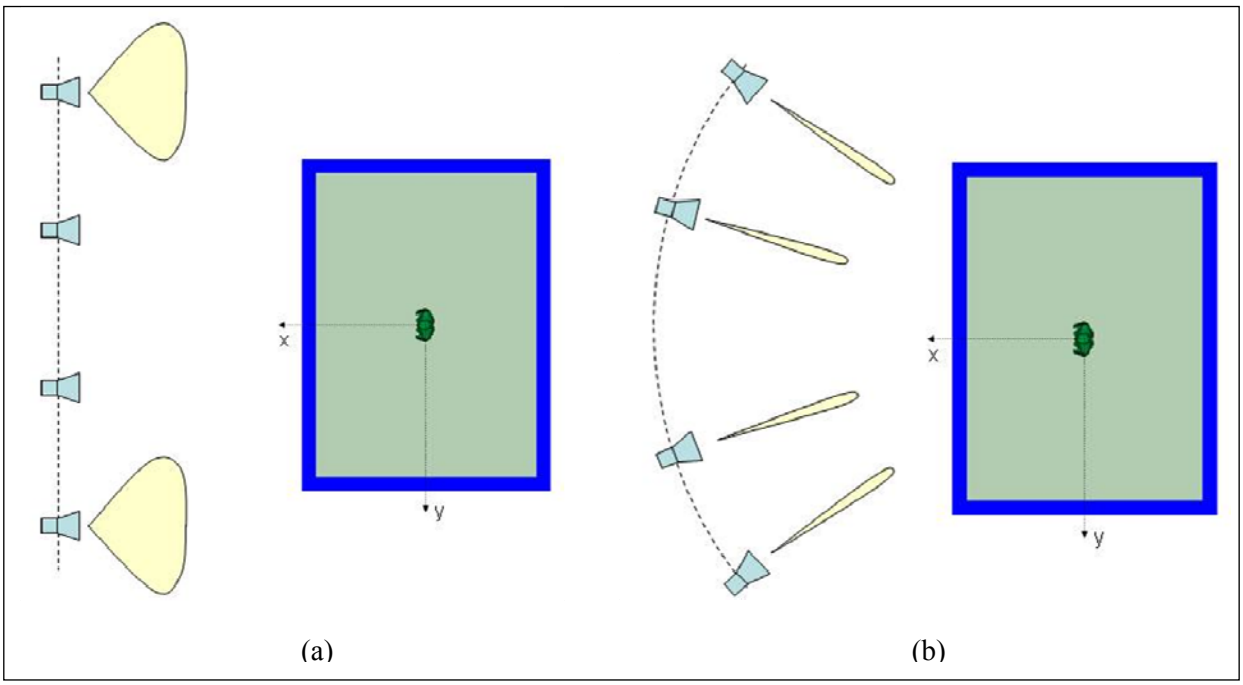

Figure 1. SAR data collection geometries: (a) strip-map mode and (b) spotlight mode.

In terms of image formation algorithms, we use two methods: the polar format algorithm (PFA) (*11, 12*) and the backprojection algorithm (BPA) (*10*). The PFA converts the data format in the frequency-angle domain from polar to Cartesian coordinates and then takes an inverse 2-D Fast Fourier Transform (FFT). This is a computationally efficient procedure, but requires certain imaging geometries in order to minimize the imaging errors (*11*). Moreover, this algorithm is normally used in conjunction with the spotlight mode. Most of our imaging examples are created by a combination of the spotlight mode and the PFA. On the other hand, the BPA is exact but computationally very intensive (*10*). In most through-the-wall radar imaging applications, the BPA is employed together with the strip-map SAR mode. In section 3.4, we compare both image

formation algorithms for a similar imaging geometry and show that carefully applying either algorithm produces similar results.

There are three SAR configurations that we employ in our numerical examples. One of them considers the spotlight mode and implements the PFA for image formation. In this case the radar is placed in the far-field and moves on a circular path (the distance to the center of the room is constant). In the models, we compute the target's response at various azimuth aspect angles using plane wave excitation (that is, infinitely narrow antenna beamwidth). In the following, we call the angular range the imaging aperture. In order to achieve downrange resolution, the target response is also computed frequency by frequency over a large bandwidth. In this respect, our simulations mimic the operation of a stepped frequency radar. The fields computed at the receiver do not include the $1/R$ term (characteristic for the spherical spread in the far-field [*19*]); therefore, the images are independent of the standoff distance between radar and target.

We should mention that this far-field geometry is ideal in conjunction with the PFA since it automatically eliminates one major source of errors, namely, the range curvature effect (*11, 12*). Nevertheless, this feature is made possible by the fact that plane wave excitation and observation can be rigorously implemented in our radar signature computer codes. In the physical world, the wavefront curvature is always present and produces phase errors within the PFA that need to be corrected (linear errors) or kept under control (quadratic errors) (*11*). If unchecked, these errors could introduce severe distortions in the image of a building (manifested for instance as wall warping) particularly since the operational frequencies are low and the target dimensions (or imaging area) are large (*11*).

One of the most important processing steps in the PFA is the polar-to-Cartesian data interpolation (*11, 12*). The original SAR data collection yields samples over a range of frequencies and azimuth angles that cover an annulus-shaped area when mapped onto the k_x–k_y plane (the wave vector components in the image plane). These data points need to be re-sampled (interpolated) onto a rectangular grid before the 2-D FFT is performed. Without getting into details of the interpolation procedure (*11, 12*), we need to mention that the choice of the rectangular data grid support has a significant impact on the image quality. The basic options are shown in figure 2: the inner (or inscribed) support (figure 2a), the outer (or circumscribed) support (figure 2b), or the midpoint support (figure 2c). The inner support reduces the image cross-range resolution to that corresponding to the lowest frequency in the spectrum, but has the best sidelobe performance. The outer support uses the full image cross-range resolution corresponding to the highest frequency in the spectrum, at the expense of creating significant image sidelobes. The midpoint support makes a compromise between the two previous methods, achieving a cross-range resolution corresponding to the center frequency and partially mitigating the effect of sidelobes. The polar-to-Cartesian interpolation is the only PFA image formation step that limits the aperture size of the imaging geometry. This becomes particularly critical in the context of employing a very large bandwidth and wide aperture. As a rule of thumb, the effective aperture should not exceed 30°. A detailed account of the interpolation configurations and their

performance is presented in Knittle et al. (*20*). We directly investigate their effect on the SAR images of a room in section 3.1.

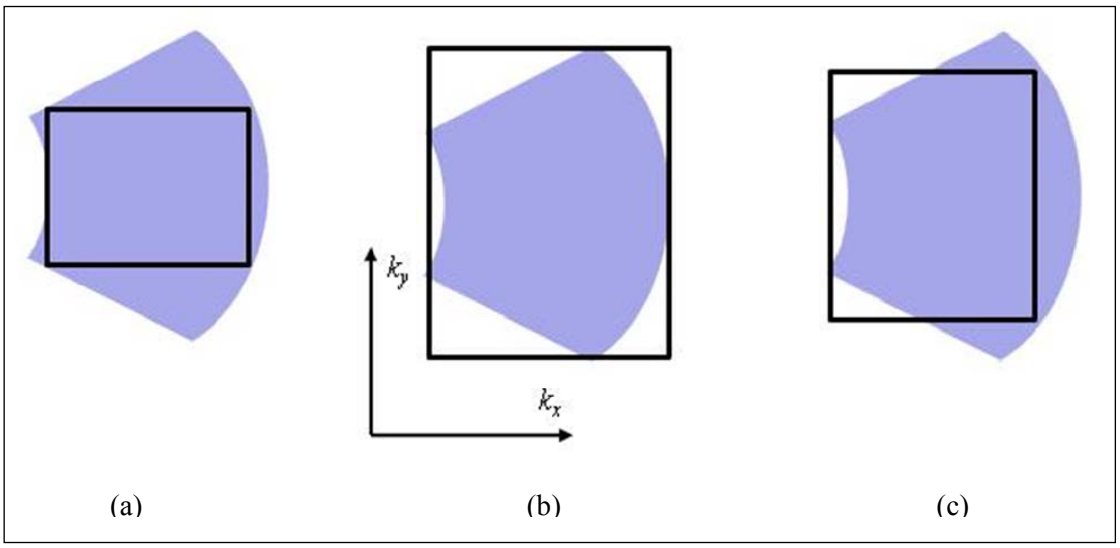

Figure 2. Different support choices for the polar-to-Cartesian interpolation procedure in the PFA: (a) inscribed, (b) circumscribed, and (c) midpoint.

The images are presented as magnitude maps in dB scale. The absolute values on the dB scales are not relevant to our analysis. However, the intensity of each image pixel is always scaled back to the number of data points in the 2-D FFT, such that we can perform a meaningful comparison between pixel intensities of images obtained from data sets with different numbers of data points. In these simulations, the elevation angle is 0° (propagation vector in the *x*-*y*, or horizontal, plane). That means the slant plane (*12*) is identical to the ground plane (and the image plane as well).

As pointed out earlier, this imaging scenario is not particularly relevant to practical implementations of STTW radar systems. One issue is that, for a target as large as a room, the near-zone field extends to large distances at typical STTW radar frequencies. Using the $2D^2/\lambda$ equation for the lower limit of the far-field zone (*19*)—where D is the largest target dimension and λ is the wavelength—we obtain 417 m for a 5-m-wide room at 2.5 GHz. At the same time, a typical sensor-to-target distance could be on the order of 10–20 m. Therefore, the far-field assumption is most likely invalid.

Nevertheless, we chose this procedure in most of our simulations because of the lower computational cost and the availability of the modeling software. All the assumptions made by the PFA are consistent with the corresponding modeling procedure (with the restriction of keeping the imaging aperture within reasonable limits). We analyze the differences between this procedure and more realistic modeling scenarios in sections 3.4 and 3.5. Despite the caveats in

this approach, we still believe that it can illustrate key phenomenological effects in predicting STTW imaging radar performance.

The image resolution is given by the range of frequencies and angles considered in the 2-D FFT according to the following equations (*12*):

$$down\text{-}range\ resolution = \frac{c}{2BW} \tag{1}$$

$$cross\text{-}range\ resolution = \frac{\lambda}{2(\phi_{\max} - \phi_{\min})} \tag{2}$$

where c is the speed of light, BW is the radar bandwidth, λ is the wavelength at the center frequency, and $\phi_{\max} - \phi_{\min}$ is the angular aperture (in radians).

In order to reduce the image sidelobes, we use Hanning windows (*21*) in both the frequency and the angular domains, as shown in figure 3. This procedure also reduces the resolution as compared to the image that would use the full aperture and bandwidth—since the Fourier transform of a Hanning window has a wider main lobe than the Fourier transform of a rectangular window. The choice of the Hanning window for aperture weighting is not necessarily optimal in achieving the sidelobe-resolution tradeoff. However, the issue of the optimal aperture weighting function is beyond the scope of this study (*12*). In figure 3a, we notice that the total bandwidth between the zero-crossing points is 4 GHz. If the entire bandwidth were used in the imaging process with a rectangular window, the downrange resolution would be 3.75 cm. However, after Hanning windowing, the resolution degrades by approximately a factor of two to 7.5 cm (notice that this is a rather conservative estimate). Following Shaeffer et al. (*22*), we call the "average" bandwidth available after windowing in the frequency domain the "effective bandwidth." In our case, this is 2 GHz. By plugging this number into the usual downrange resolution calculation formula, we obtain the correct value of 7.5 cm. Similarly, we define the "effective aperture" as the "average" aperture available after windowing in the angular domain. Throughout this report, we always list the effective bandwidth or aperture when we describe the parameters of a certain SAR image. One should keep in mind that the underlying data, in terms of frequencies or angles, extend twice as much as the effective bandwidth/aperture.

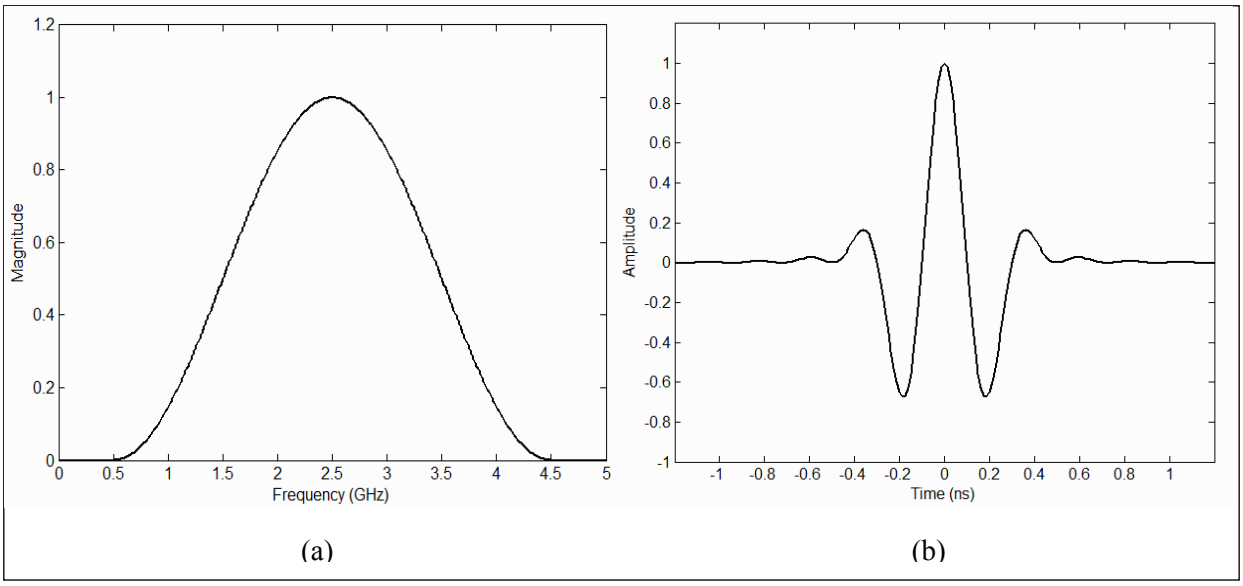

Figure 3. Hanning window and its Fourier pair: (a) frequency domain and (b) time domain.

A second approach to simulating a room imaging system consists of computing the radar data for spotlight geometry, converting it to an equivalent strip-map configuration and applying the BPA for image formation. In this case, we assume that the radar transmits and receives at points with well-defined Cartesian coordinates along the linear synthetic aperture, and find the relative angle made by each pixel in the image with each antenna position. The intensity of one image pixel is obtained by (coherently) adding the contributions of all the samples along the synthetic aperture. The latter are found through a look-up procedure using the spotlight radar data obtained for the entire possible angular range. The far-field data generated by modeling the spotlight geometry can be corrected to account for the sidelobe-reduction angular window mentioned in the previous paragraph (notice that the antenna pattern of a real strip-map SAR system would naturally provide this tapering at the edges of its beam; however, when we convert the far-field spotlight data, we have to artificially introduce this step in post-processing). Since the BPA operates directly in the time domain, we need to match the excitation pulse spectrum to the inverse Fourier transform of the desired frequency domain window described previously (an example is shown in figure 3). We should note that this image formation method is not identical (although it is related) to the tomographic backprojection algorithm (*12*) employed in spotlight SAR. Overall, this approach is more realistic than the spotlight/PFA procedure, except for the fact that we still do not account for the antenna elevation pattern (in our scenario, the transmitted/received radar waves still propagate uniformly at 0° elevation).

The third approach removes this inconsistency by performing near-field radar scattering simulations with the antenna placed at specific locations along the linear synthetic aperture (pointing in the same direction) and applying the BPA for image formation. This model directly simulates a strip-map configuration and can only be performed with Xpatch, as explained in section 2.1. The antenna is always pointing in the same direction and has a pattern (both in

elevation and azimuth) specified by the user. The image is created in a horizontal (x-y) plane placed at the antenna height. The intensity of one image pixel at coordinates (x, y, z) (where z is the image plane height) is obtained by coherent summation of contributions from all samples along the synthetic aperture (and possibly applying an angular window), according to the following equation:

$$I(x,y,z)=\left(\left[\sum_n w(\phi_n)s_n(t+\tau_n(x,y,z))\right]*h(t)\right)_{t=0} \tag{3}$$

$$\tau_n(x,y,z)=2\frac{(x-x_n)^2+(y-y_n)^2+(z-z_n)^2}{c} \tag{4}$$

where n represents the sample index along the synthetic aperture; (x_n, y_n, z_n) are its coordinates; $s_n(t)$ is the time-domain signal received by the radar at position n; $w(\phi_n)$ is the aperture weighting function depending on the azimuth direction of the pixel; $\tau_n(x, y, z)$ is the wave propagation time from the transmitter at position n to the pixel at (x, y, z) and back to the receiver at position n; and $h(t) = p^*(-t)$ is the impulse response of the filter matched to the transmitted waveform $p(t)$. Notice that, for our particular geometry, $z - z_n = 0$. Although this formulation assumes monostatic radar operation, it can be easily extended to bistatic configuration.

Since we simulate the operation of a stepped frequency radar, we can choose between two ways of implementing the BPA: (1) taking inverse FFTs of the frequency domain data to form range profiles and then performing the delay and sum operations or (2) implementing the algorithm directly in the frequency domain according to the following equation (*10*):

$$I(x,y,z)=\sum_n w(\phi_n)\int_\omega S_n(\omega)P^*(\omega)\exp(j\omega\tau_n(x,y,z))d\omega \tag{5}$$

where $S_n(\omega)$ is the spectrum of the received signal at position n and $P(\omega)$ is the transmitted waveform spectrum. In section 3.5, we employ the first of the two implementations.

The matched filter operation described in equation 3 is typically employed in chirp radar (*10*) in order to form range profiles based on the received signals. In our case, the range profiles are constructed by simply taking the inverse Fourier transform of the stepped frequency responses of the target over a large bandwidth, weighted by the desired excitation spectrum. Therefore, in our implementation of the BPA, we skip the matched filter operation. This type of image formation procedure is known as delay-and-sum.

If we used the entire synthetic aperture length, the cross-range resolution for a strip-map configuration would be given by the following (*10*):

$$cross\text{-}range\ resolution=\frac{R\lambda}{2L} \tag{6}$$

where R is the aperture to target range and L is the synthetic aperture length, while the downrange resolution equation remains the same as equation 1. However, since our BPA implementation uses a constant integration angle for each pixel in the image (which is limited by the antenna beamwidth), it is more accurate to use equation 2 when evaluating the cross-range resolution in this scenario. More details on this type of simulation are presented in section 3.5.

Finally, we need to mention that, throughout this work, we compute the delays $\tau_n(x, y, z)$ as for free-space propagation. However, due to the propagation mechanisms through walls, this delay estimate is inexact and the images of targets placed in a room appear at location behind their real position, in addition to being slightly de-focused. This effect is more severe for wall materials with a large dielectric constant, such as concrete. While the offset in behind-the-wall target localization may not be an issue in some applications, it could create problems for detection algorithms attempting to fuse images taken from different viewpoints (*23*). If one has a priori knowledge of the wall thickness, dielectric constant, and attenuation, the target position can be fully compensated for by calculating the exact time delays $\tau_n(x, y, z)$ upon propagation and scattering through the wall (*23*). If the wall parameters are unknown, several techniques can be employed to correct the images. One can attempt to estimate the wall parameters directly from the radar data (*24*). Another approach is to autofocus the image through an iterative process by trying to optimize a certain image quality metric (*25*). A third approach involves creating images from two standoff distances and a range of wall parameters, and finding the intersection points of the target trajectories under these conditions (*26*). All these techniques are beyond the scope of this report.

2.3 Computational Meshes

The computational meshes used in our simulations consist of four-wall simple rooms with various targets placed inside. We start with very realistic computer aided design (CAD) models and convert them to either volumetric grids made of small cubic cells for AFDTD simulations or triangular facet meshes that represent the outer shell of objects for Xpatch simulations.

In figure 4, we represent the simple room with a human placed in the middle. The room's outer dimensions are 5 m by 3.5 m by 2.2 m. All walls are 0.2 m thick. We also add a 0.15-m-thick ceiling and floor (see reference 4 for a detailed discussion on why the floor and ceiling are important to the EM modeling). In figure 4a, the ceiling and floor appear in yellow. In most simulations, when we use plane-wave excitation at 0° elevation, the room is placed in free-space, meaning there is no infinite ground plane that extends beyond the room's footprint. This is dictated by the fact that a plane wave propagating at 0° elevation in the presence of an infinite ground plane would produce null total fields everywhere in the space. However, for the near-field simulations in section 3.5, we must add an infinite dielectric ground plane (with $\varepsilon_r = 6.9$, $\varepsilon'' = 0.9$) in order to study some important phenomenological effects. The FDTD grid has a resolution (cubic cell size) of 5 mm, and its overall size is on the order of 780 by 1020 by 500 cells. For Xpatch, meshing the uniform walls is a trivial task (each wall face is made out of two

triangles). However, it is the human mesh that requires a large number of triangles: ~35,000 facets with an average edge size of 1 cm.

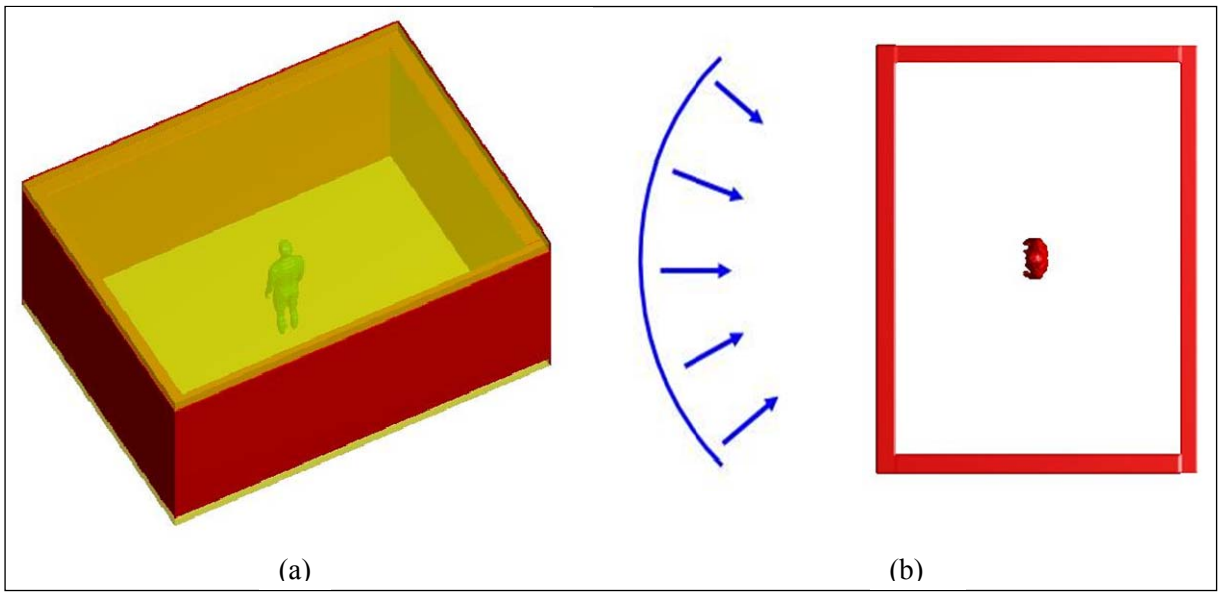

Figure 4. The simple room with homogeneous walls and a human in the middle: (a) perspective view and (b) top view showing the spotlight SAR geometry.

We investigate three different construction materials for the walls: brick, concrete, and cinder blocks. The brick walls are made of a uniform dielectric with $\varepsilon_r = 3.8$. For the dielectric loss, due to built-in limitations, we must use different models in the two codes. Thus, AFDTD can only model constant conductivity materials (conductivity independent of frequency), whereas Xpatch can only model materials with constant imaginary part of the complex permittivity. (Note: The Xpatch model is closer to real material behavior.) Notice that we match the two models at 2.5 GHz, which is the center frequency in most of our simulations. For brick, we use $\sigma = 0.03$ S/m for AFDTD, and $\varepsilon'' = 0.22$ for Xpatch (*27–30*). The concrete walls are also uniform, with $\varepsilon_r = 6.8$ and $\sigma = 0.1$ S/m for AFDTD or $\varepsilon'' = 0.9$ for Xpatch (*27–30*).

A schematic representation of a cinder block, as well as a top view of the entire room with cinder block walls, is shown in figure 5. Note that, when the cinder blocks are properly aligned, they form “air tubes” that run continuously along the wall height. In this case, the building material is again concrete, with the same dielectric properties as listed previously. In all cases, the ceiling and floor are made of uniform concrete.

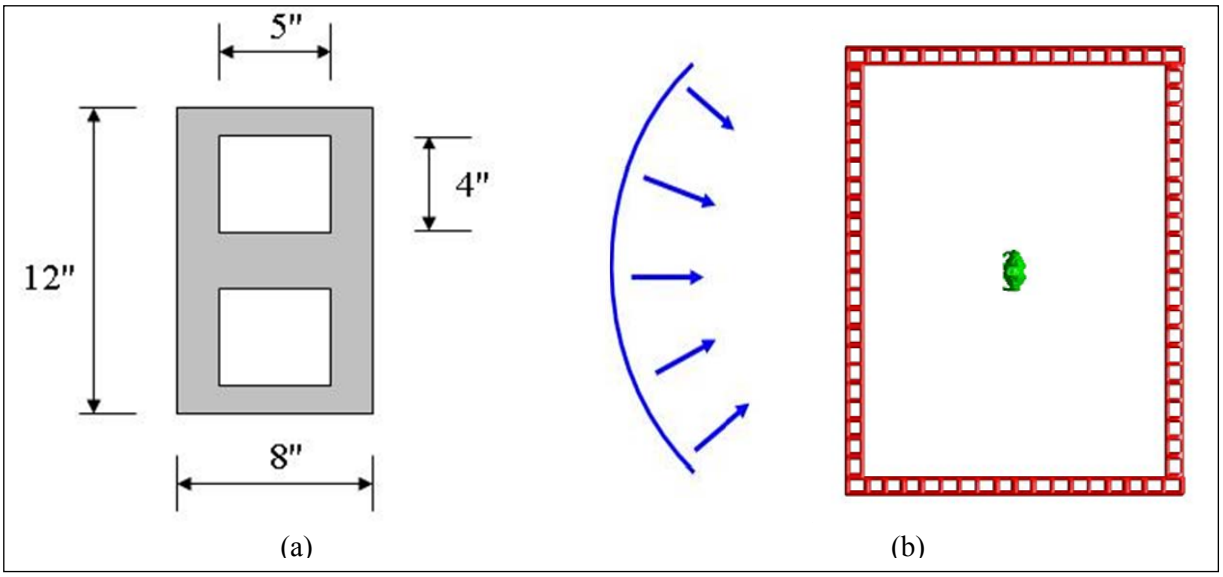

Figure 5. (a) Individual cinder block and (b) the top view of the simple room with cinder block walls and a human in the middle.

The human mesh represents the "fit man," as described in reference 1. Since this model does not include the internal structure of the body, but only the exterior shell, we must assume that the entire body is made of the same uniform dielectric material (for a discussion of the uniform dielectric human body model's validity see references 1 and 3). For this material, we picked dielectric properties close to those of skin: $\varepsilon_r = 50$ and $\sigma = 1$ S/m for AFDTD or $\varepsilon'' = 12$ for Xpatch. The AFDTD and Xpatch models of the human body have been previously analyzed in detail and validated (*1, 3*).

In section 3.7, we image a simple four-wall room that includes a metallic file cabinet and a human (figure 6). The human and cabinet meshes are centered 1 m away from the middle of the room along the *y*-axis (one in the positive and the other in the negative *y* directions). The file cabinet looks roughly like a rectangular box made of perfect electric conductor (PEC), although we included some details in the model (such as the drawer handles). The room dimensions and structure are identical to those of the model described in figure 4. Also, we consider two types of wall materials, brick and cinder block. The AFDTD grid has the same cell size and number of cells as the one in figure 4.

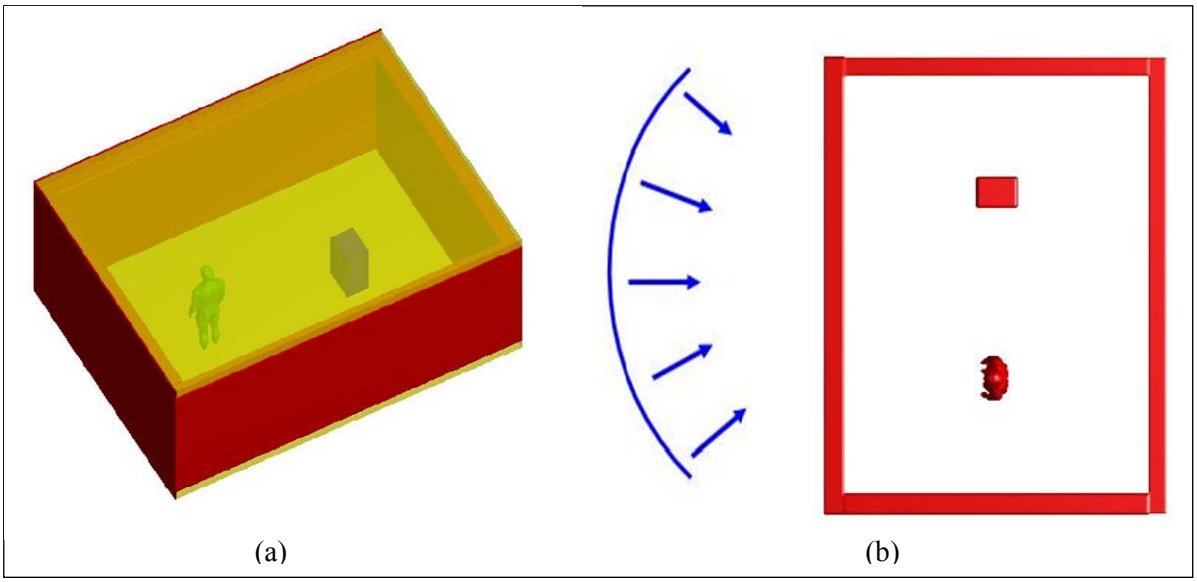

Figure 6. The simple room with homogeneous walls and a human in the middle: (a) perspective view and (b) top view showing the spotlight SAR geometry.

The spacing between two samples in the frequency and angular domain are given by the overall room (or image) dimensions according to the following equations (*12*):

$$\Delta f = \frac{c}{2\left(x_{\max} - x_{\min}\right)} \tag{7}$$

$$\Delta \phi = \frac{\lambda}{2\left(y_{\max} - y_{\min}\right)} \tag{8}$$

where $x_{\max} - x_{\min}$ is the downrange room dimension and $y_{\max} - y_{\min}$ is the cross-range room dimension. For the room in figure 4, we obtain $\Delta f = 42.8$ MHz and $\Delta \phi = 0.38°$ (at 4.5 GHz, which is the maximum frequency in the models). In our simulations, we oversample the data in both domains by choosing $\Delta f = 6.67$ MHz and $\Delta \phi = 0.25°$.

The EM models were run at the U.S. Army Major Shared Resource Center (MSRC) (*31*) on Linux Networx Evolocity II clusters. For one AFDTD run (one angle, all frequencies and all polarizations), we used 24 processors with a wall-clock run-time of ~18 h. In order to run 180 separate angles, the total CPU time was ~80,000 h. Xpatch is a much more efficient code (typically 100 to 1000 faster than AFDTD for a similar problem). It took ~120 CPU hours to obtain the far-field data for one room image with Xpatch. The near-field Xpatch simulations are significantly slower than the far-field. Thus, it took ~1,200 CPU hours to obtain the near-field data for one room image with Xpatch. The SAR images in this report based on the PFA were created using the Pioneer RCS software. The images based on the BPA were created using custom software developed at ARL.

3. Results

3.1 The Human in a Simple Room

In this section we consider the human in a simple room with uniform walls. The radar signature is computed by AFDTD. The SAR images are obtained by the PFA using a spotlight configuration. The images represent views from the top in the *x*-*y* plane, which coincides with the slant plane in our case. Downrange is represented along the *x*-axis and cross-range is represented along the *y*-axis. That means the aperture is always centered at a direction along the *x*-axis and looking from left to right (this corresponds to the azimuth $\phi = 0°$). The distances on both axes are in meters. The pixel intensities (in dB) are mapped onto a pseudo-color scale. Also, the mesh contours are overlaid in grey on top of the image to indicate the true object location.

In figure 7, we show the images of the brick-wall room centered at broadside relative to the longest side of the room for vertical-vertical (V-V) and horizontal-horizontal (H-H) polarizations. Next to each room image we include a zoomed-in section of the image area around the human. For these images, the center frequency is 2.5 GHz, with a bandwidth of 2 GHz, and the aperture is 22.5°. Using equations 1 and 2 to evaluate the image resolution, we obtain a 7.5-cm downrange resolution and 15-cm cross-range resolution. The major features in these images are the front and back sides of the front wall, the front and back sides of the back wall, and the human in the middle. There is also another faint vertical line (behind the return from the back side of the front wall) that represents the double round-trip of the radar waves through the front wall. An additional feature is the small gap in the middle of the back wall that appears as a shadow of the human. This phenomenon is explained in detail in the appendix. Notice the displacement of all the objects behind the front wall (including its back side), caused by the fact that we do not compensate the image for the slower wave velocity inside the wall dielectric material (see reference 4 for a more detailed analysis of these delays). It is interesting to record the highest intensity pixel for some of these features. Thus, for the front side of the front wall we obtain –1.9 dB for V-V polarization (–1.8 dB for H-H), whereas for the back side of the front wall we obtain –15.1 dB (both polarization). For the human image, we have a peak of –27.9 dB for V-V polarization (–28.1 dB for H-H). It is apparent from these results that there are no major differences between the vertical and horizontal polarizations, which is consistent with our previous investigations of the radar return from both humans (*1*) and rooms (*4*). We noticed this to be the case for all the other scenarios considered in this report, when the aperture is centered at broadside.

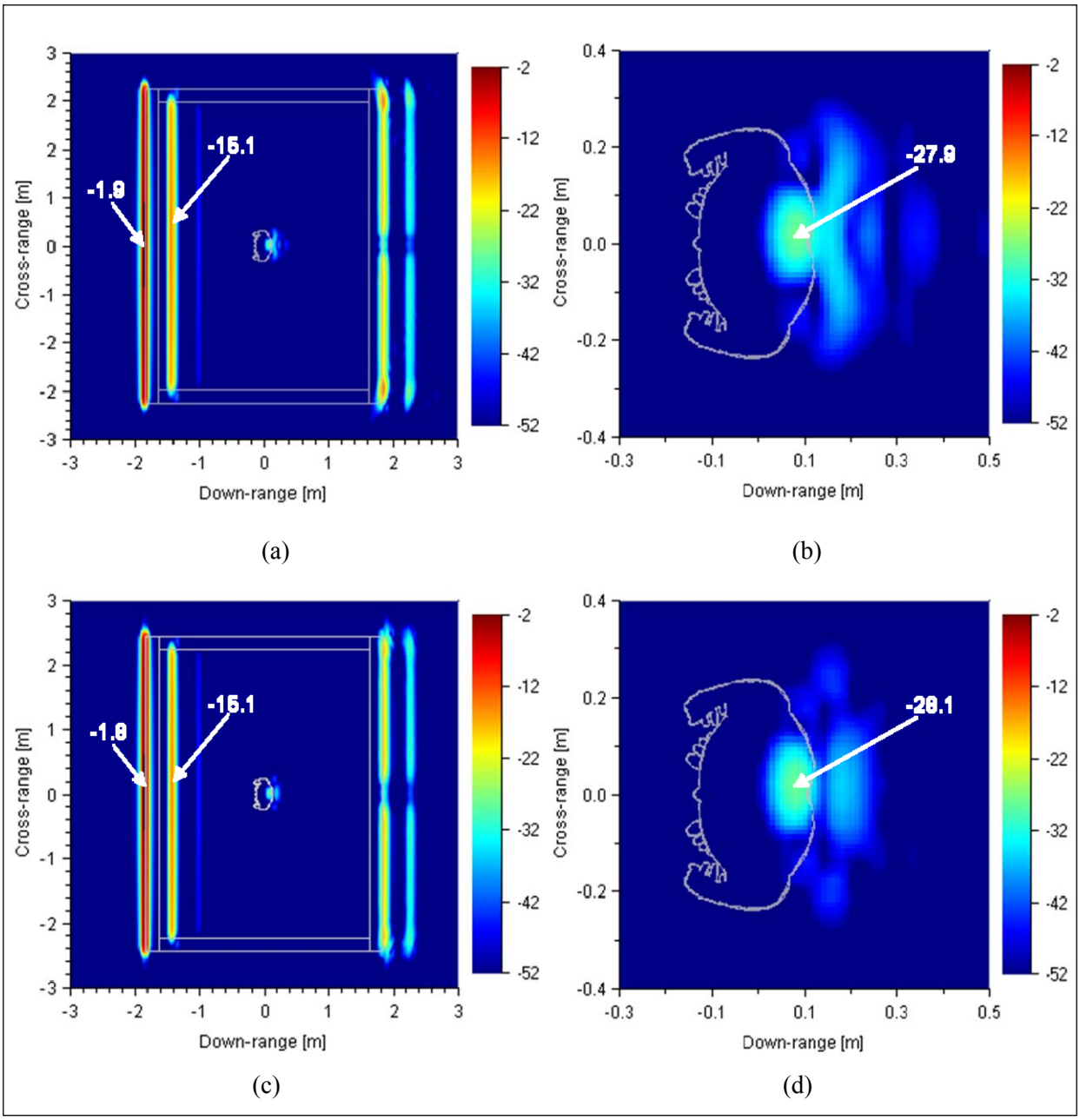

Figure 7. SAR images of a simple room with brick walls, obtained for spotlight mode and the PFA from AFDTD data, 2 GHz bandwidth centered at 2.5 GHz and 22.5° aperture centered at broadside, showing (a) V-V polarization, entire room; (b) V-V polarization, detail around the human; (c) H-H polarization, entire room; and (d) H-H polarization, detail around the human.

Figure 8 makes a comparison between the various polar-to-Cartesian interpolation methods described in section 2.2, using the same room and the same imaging parameters as previously described. The image in figure 8a, obtained using the inner support method, does not exhibit visible sidelobes around the wall corners, but the image's cross-range resolution is clearly degraded (notice the sideways smearing of the front wall). This effect is significant since we use a very wide frequency band and a very large aperture size. Consequently, the inner support method throws away a large amount of data, narrowing the effective imaging aperture. The image in figure 8b (using the outer support method) displays good cross-range resolution, but exhibits visible sidelobes around the back wall corners. It is interesting that the sidelobe lines make an angle of 22.5° with the back wall, being perpendicular to the propagation direction at the aperture edges (*20*) (recall that the full aperture runs from –22.5° to 22.5°). Finally, figure 8c, obtained using the midpoint method, achieves a good tradeoff between resolution and sidelobes. All the other PFA images in this report employ the midpoint interpolation method.

In figure 8d, we illustrate the effects of insufficient angular sampling rate on the SAR image of a room. In this image, we used a 0.5° increment for aperture sampling. We notice the front wall grating lobes (fuzzy lines that appear as continuations of the wall) that were not present in figure 8c (the image in figure 8d also uses the midpoint interpolation method). The grating lobes are a clear illustration of aliasing (*21*) due to angular sampling below the Nyquist rate given by equation 8. In real SAR systems, this effect can be avoided by achieving a high enough pulse repetition frequency (PRF) (*12*).

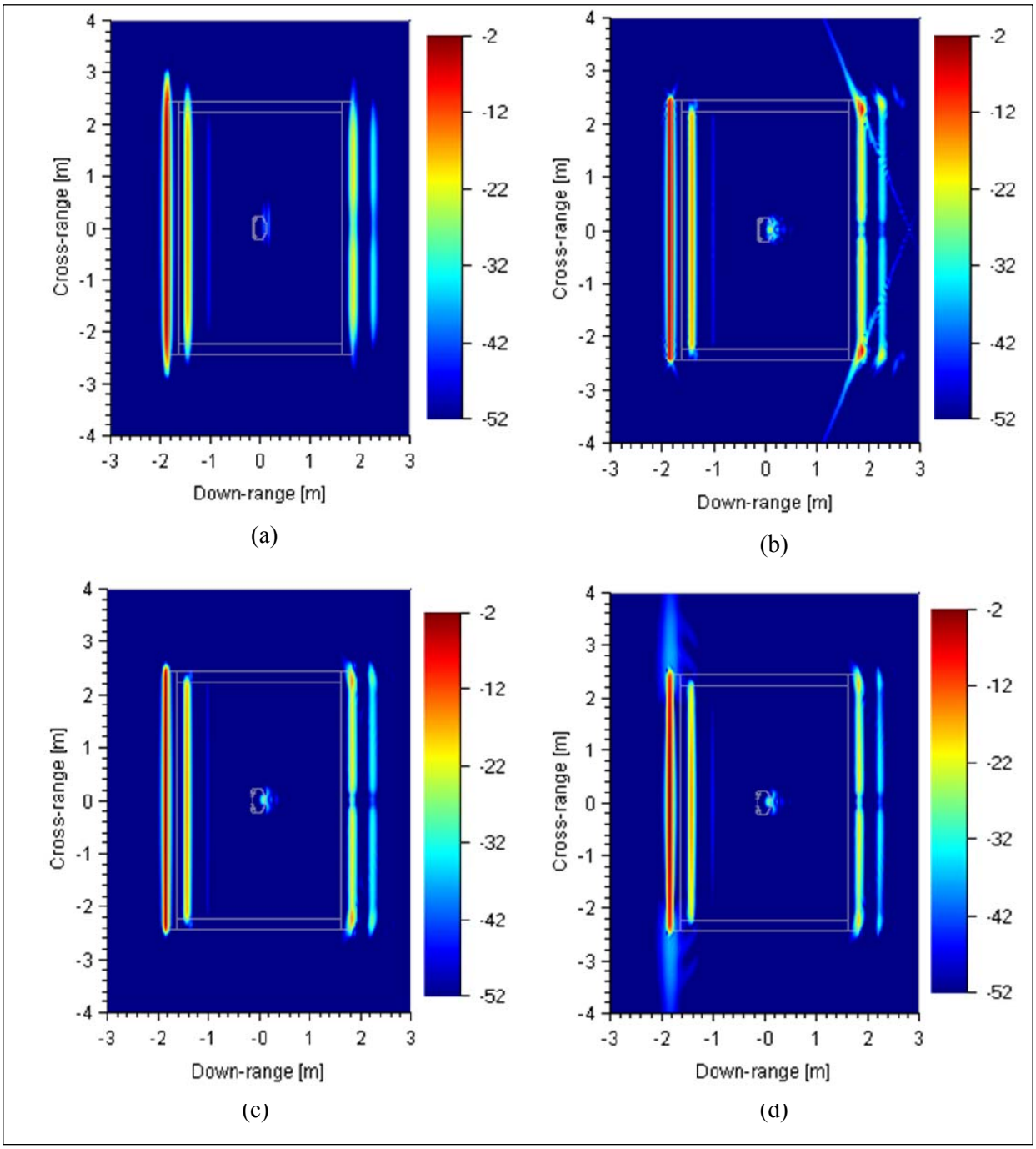

Figure 8. SAR images of a simple room with brick walls, obtained for spotlight mode with the PFA from AFDTD data in V-V polarization, 2 GHz bandwidth centered at 2.5 GHz and 22.5° aperture centered at broadside, showing the effects of (a) inscribed interpolation, (b) circumscribed interpolation, (c) midpoint interpolation, and (d) insufficient angular sampling (0.5°).

We should emphasize that the sidelobe issue may have a significant impact on trying to detect targets within the SAR image of a room or building. The reason is that typical targets and objects in the scene may display a wide dynamic range and may only be separated by short distances (e.g., weak human target placed close to a bright wall). Therefore, a radar imaging system for this application must be carefully designed to minimize the image sidelobes.

Figure 9 presents the images of the same brick-wall room, this time for a 22.5° aperture centered at 45° with respect to the walls (the center frequency is 2.5 GHz and the bandwidth is 2 GHz). The first observation is that the walls disappear from the image (since the wall specular reflections are directed away from the radar). The only features that show up in these images are the room's vertical corners and the human. Interestingly, we can distinguish both the front and the back sides of each corner, and moreover, for the inside corner (the farthest from the radar and also the brightest in the image) we can see the echoes produced by multiple reverberations inside the walls. The peak intensity in the images in figure 9 occurs for the inside corner. This time there is a significant difference between the two polarizations: 1.4 dB for V-V and –10.3 dB for H-H. This result is in line with the scattering analysis of an inside vertical wedge (*19*). However, the other features in the image, such as the human and the other corners of the room show rather similar intensities for the two polarizations (the human peaks at –37.4 dB for V-V and –33.7 dB for H-H). Another important feature of the images in figure 9 is the presence of ghost images, around the points where the human projects onto the two back walls (the walls farthest from the radar). This problem is analyzed in detail in the appendix.

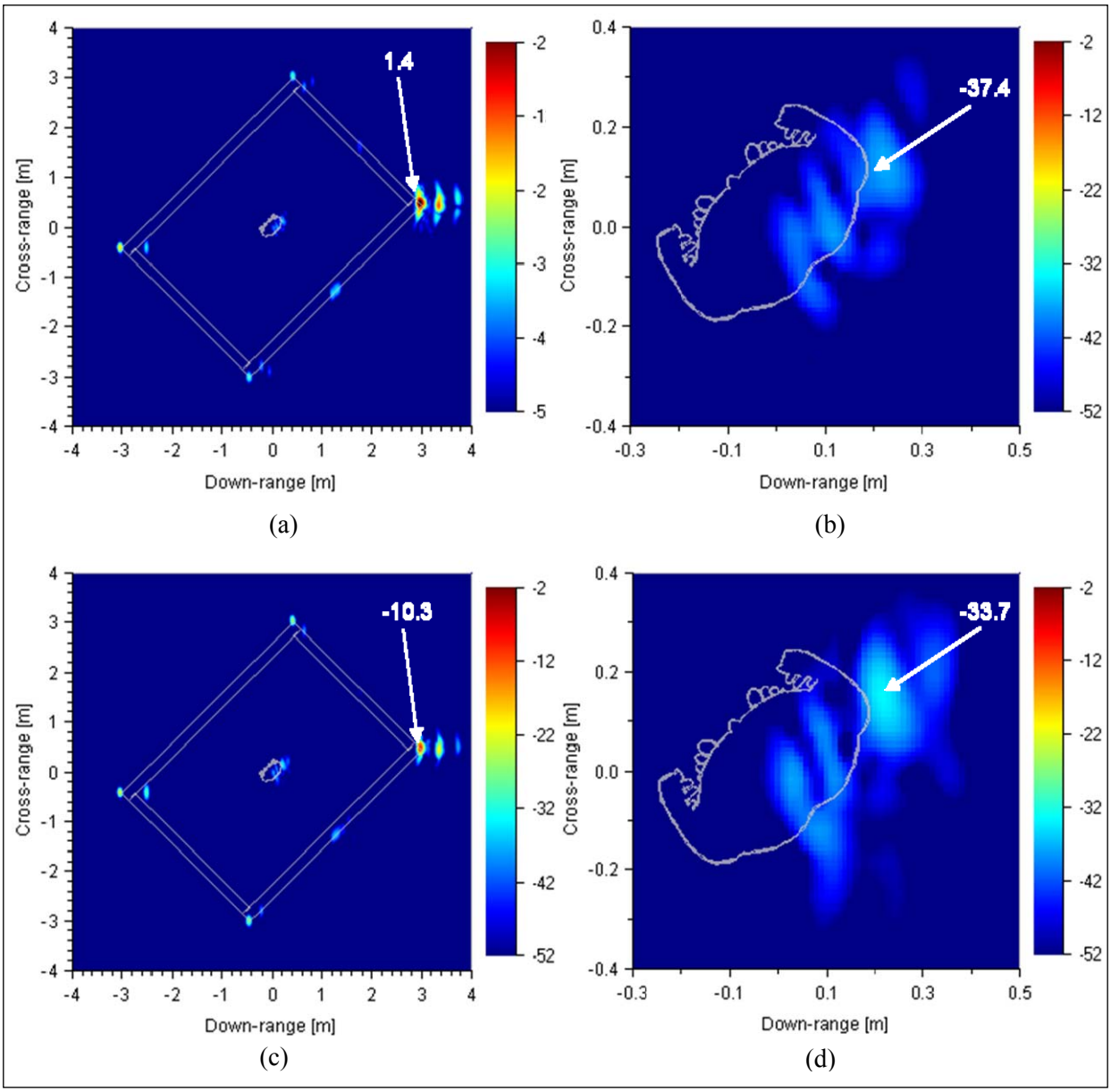

Figure 9. SAR images of a simple room with brick walls, obtained for spotlight mode and the PFA from AFDTD data, 2 GHz bandwidth centered at 2.5 GHz and 22.5° aperture centered at 45°, showing (a) V-V polarization, entire room; (b) V-V polarization, detail around the human; (c) H-H polarization, entire room; and (d) H-H polarization, detail around the human.

Although imaging at an oblique angle represents a somewhat contrived scenario for a vehicle-based STTW radar that takes SAR images in a drive-by operational mode, the results presented here suggest that such a configuration could eliminate the walls from the image. In order to achieve this, the imaging aperture must not include incidence at an angle perpendicular to the room's walls. Another reason for presenting this case is to clearly emphasize the issue of the ghost images, which is related to multiple scattering inside the room.

We also show the case of a room with uniform concrete walls. This is a very challenging scenario for detecting targets inside the room, since the attenuation through the walls is very severe, about 40 dB for a round-trip of around 2.5 GHz (*32*). The SAR images obtained in this case are shown in figure 10. The radar parameters are identical to the previous examples, with the aperture centered at broadside. One notices that high dynamic range is required for detection of targets behind concrete walls. Also, since concrete has a higher dielectric constant than bricks, the targets are displaced further from their real locations in the case of concrete walls.

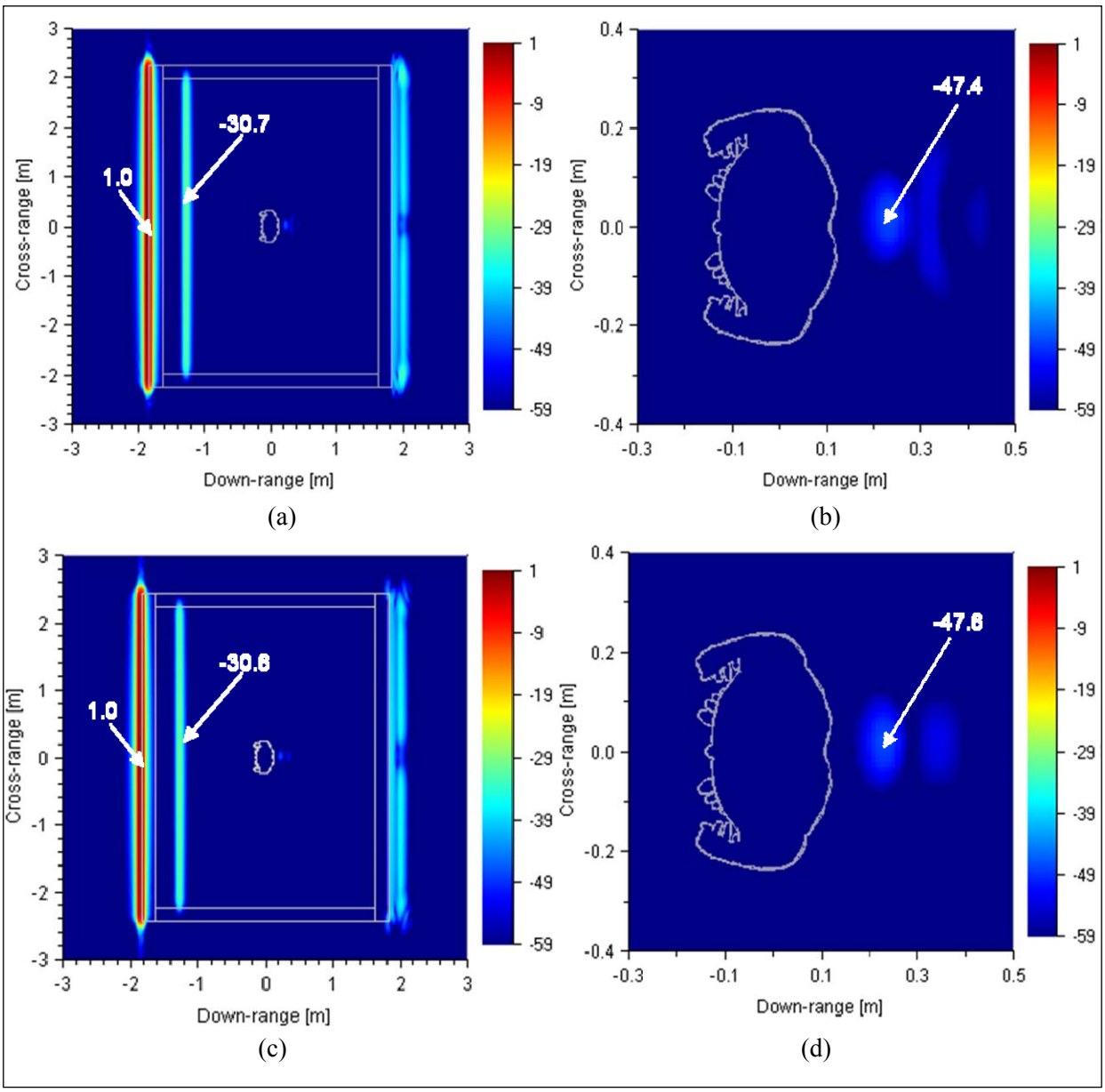

Figure 10. SAR images of a simple room with concrete walls, obtained for spotlight mode and the PFA from AFDTD data, 2 GHz bandwidth centered at 2.5 GHz and 22.5° aperture centered at broadside, showing (a) V-V polarization, entire room; (b) V-V polarization, detail around the human; (c) H-H polarization, entire room; and (d) H-H polarization, detail around the human.

3.2 The Human in a Cinder Block Room and Imaging Parameter Trade-off

In figures 11 through 14, we present the SAR images obtained for the human placed in the middle of a simple four-wall cinder block room for an aperture centered at broadside and V-V polarization (the configuration and algorithms are the same as in section 3.1). These figures illustrate the effect of modifying the radar bandwidth and center frequency on the image quality. As a baseline case, in figure 11, we use a 1-GHz bandwidth centered at 1.5 GHz. In figure 12, the bandwidth is still 1 GHz, but this time centered at 2.5 GHz. In figure 13, we increase the bandwidth to 2 GHz centered at 2.5 GHz. Finally, in figure 14, we have a bandwidth of 1 GHz, but increase the center frequency to 3.5 GHz. Generally, the larger bandwidth increases the downrange resolution, whereas the larger center frequency increases the cross-range resolution. In all cases, we consider a 30° aperture centered at broadside. Next to the full room images, we show zoomed-in sections of the image area around the human. Notice that we always use the same image dynamic range in order to make direct comparisons between images.

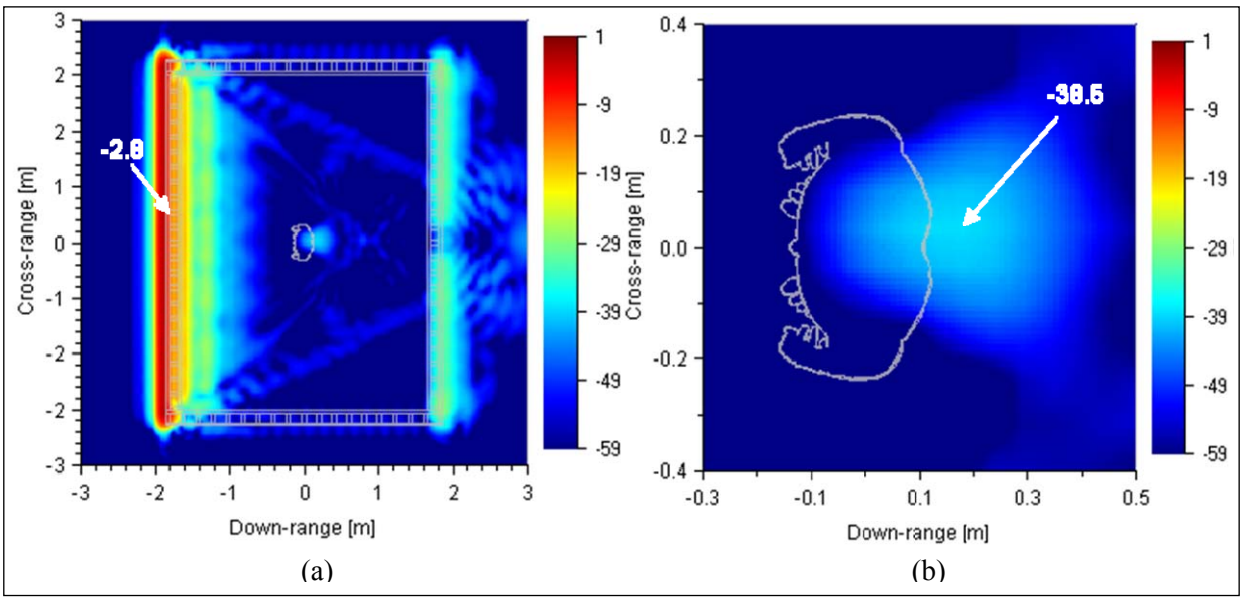

Figure 11. SAR images of a simple room with cinder block walls, obtained for spotlight mode and the PFA from AFDTD data, 1 GHz bandwidth centered at 1.5 GHz and 30° aperture centered at broadside, V-V polarization, showing (a) the entire room and (b) detail around the human.

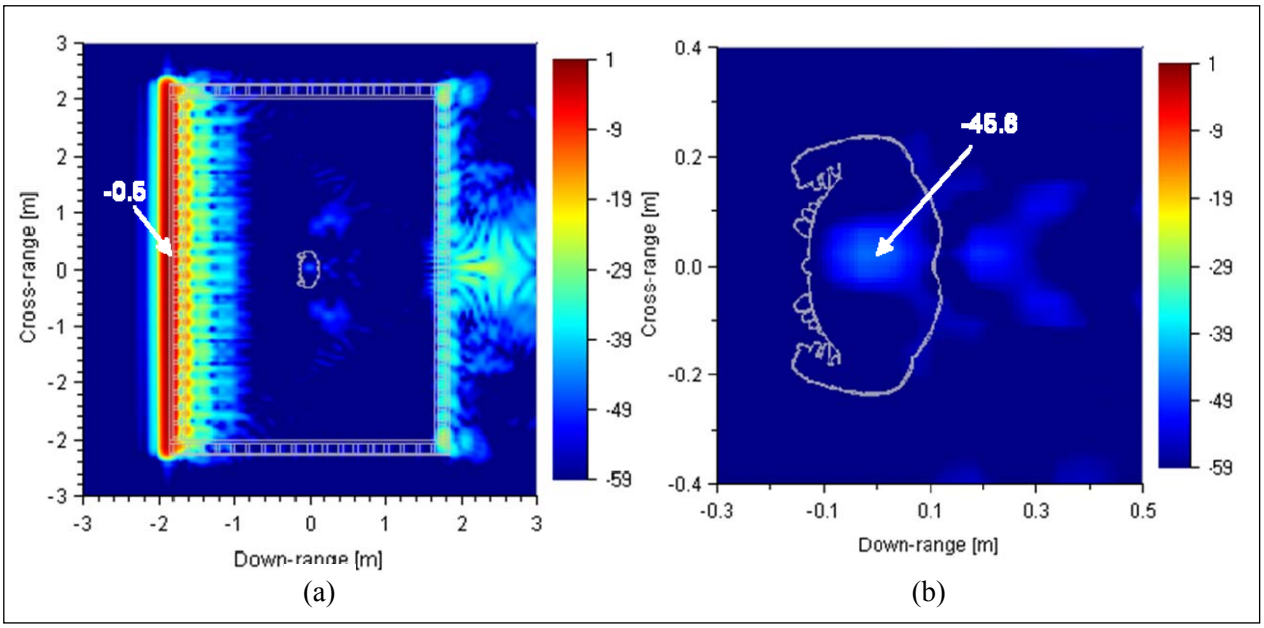

Figure 12. SAR images of a simple room with cinder block walls, obtained for spotlight mode and the PFA from AFDTD data, 1 GHz bandwidth centered at 2.5 GHz and 30° aperture centered at broadside, V-V polarization, showing (a) the entire room and (b) detail around the human.

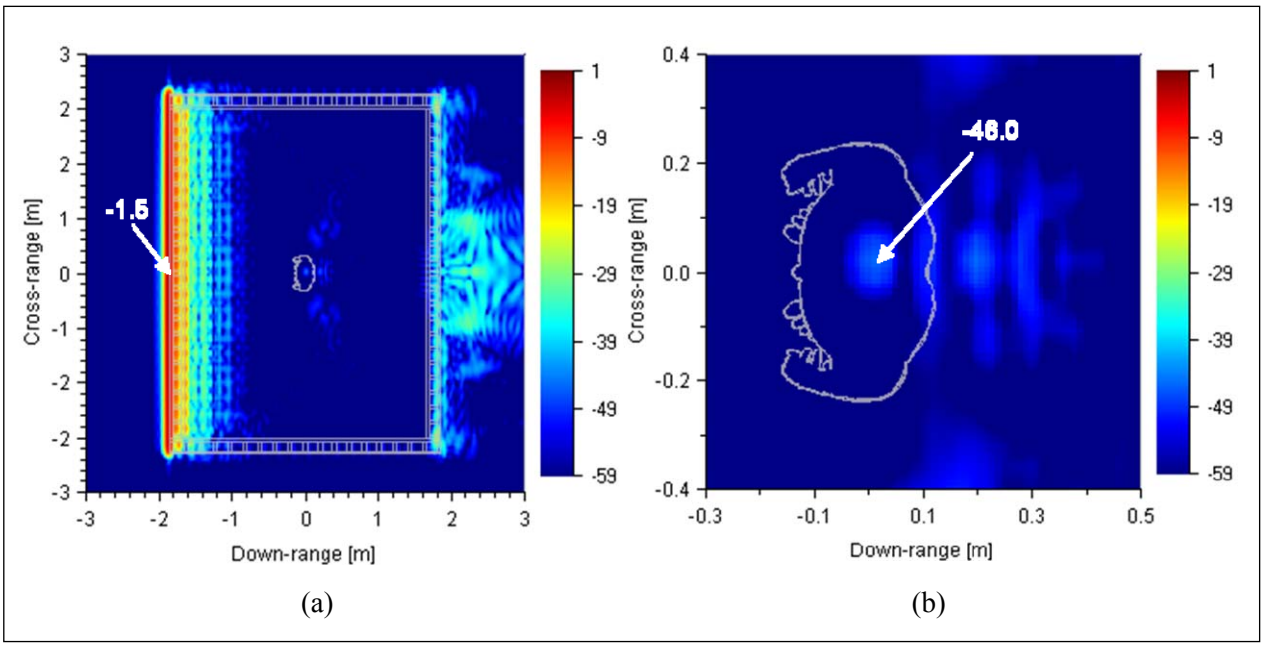

Figure 13. SAR images of a simple room with cinder block walls, obtained for spotlight mode and the PFA from AFDTD data, 2 GHz bandwidth centered at 2.5 GHz and 30° aperture centered at broadside, V-V polarization, showing (a) the entire room and (b) detail around the human.

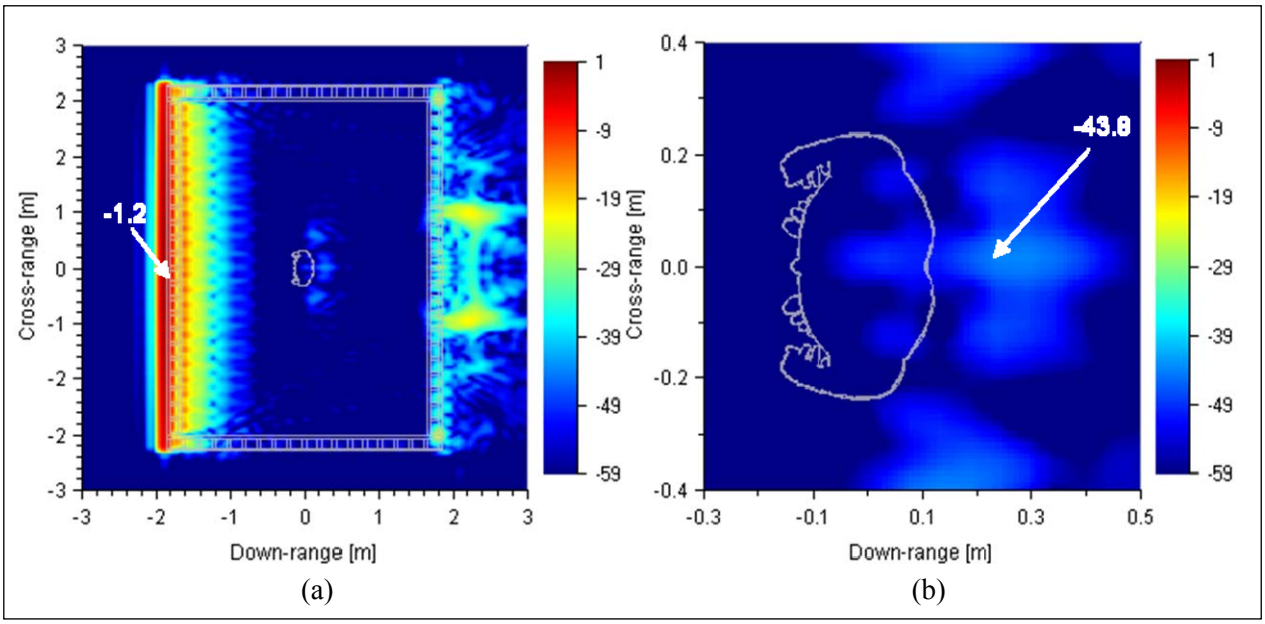

Figure 14. SAR images of a simple room with cinder block walls, obtained for spotlight mode and the PFA from AFDTD data, 1 GHz bandwidth centered at 3.5 GHz and 30° aperture centered at broadside, V-V polarization, showing (a) the entire room and (b) detail around the human.

A feature common to all the images obtained for the cinder block room is the "smearing" of the front wall image, caused by the multiple bounces of the radar waves inside the cinder block air gaps. This effect suggests that it would be extremely challenging to detect any target placed close to the wall, based on static SAR images alone. Also, we notice that the pattern created by this particular wall geometric structure in the image domain is better resolved as we increase the bandwidth (figure 13 as compared to figure 12). There is also an increased amount of clutter inside the room (compared to the brick wall room) that can be attributed to the propagation through the non-uniform walls. Moreover, we notice that some of this clutter is created by propagation through the side walls. In figures 11 through 14, we tried to set the lower limit of the dB scale such that we reduce the visible amount of clutter in the image without completely erasing the human image. The large artifact that we see just behind the back wall, in the middle, is the effect of the multipath scattering (ghost image) issue discussed in the appendix. This time, the ghost image has generally a more complex pattern and is less localized than in the brick room case, due to the more complex reflection and scattering phenomena that occur along the back wall (figure 13). Interestingly, at lower frequencies (figure 11), the ghost image becomes again more localized and appears simply as a shadow on the back wall image (similar to the brick room case).

In figures 12b, 13b, and 14b, we notice multiple images of the human, caused by the radar waves travelling multiple paths due to reverberations inside the cinder block walls. The increased bandwidth (figure 13b) or center frequency (figure 14b) allows for resolving the multiple images—in downrange (figure 13b) or cross-range (figure 14b), as opposed to the case in

figure 11b (lower frequency and bandwidth). This effect can be confusing to a human detection scheme based on the SAR images. Also, in the case shown in figure 11, the lower frequencies have better penetration properties through the lossy walls; therefore, the human image appears brighter (compared to figures 12b, 13b, and 14b). At the same time, we notice a degradation of image resolution, manifested as smearing of both the front wall and the human images. Nevertheless, this example suggests that, in certain cases, sub-banding the radar return may actually increase the chances of correctly detecting a target inside the room.

3.3 Comparison between FDTD and Xpatch Simulations of SAR Images of Rooms

The purpose of this section is to validate Xpatch models of radar scattering by a room, looking at the accuracy and limitations of this approximate EM solver in simulating the type of problems investigated in this report. A detailed analysis of Xpatch radar range profiles obtained from a simple room with a human inside has been presented previously (*4*). In this report, we focus our attention to SAR images of the simple room. This study is motivated by the fact that in certain STTW scenarios, using FDTD models may be computationally prohibitive or impractical, and in those cases, Xpatch can offer a quick and relatively accurate evaluation of radar performance. Also, as seen in section 3.5, Xpatch can provide near-field radar signature models, while the AFDTD code does not have this capability.

The images presented in this section have the same format and are computed by the same methods as in section 3.1. We analyze the following scenarios: brick room with aperture centered at broadside (figure 15), brick room with aperture centered obliquely at 45° (figure 16), and cinder block room with aperture centered at broadside (figure 17). As in the previous sections, we include zoomed-in image areas around the human. The radar parameters are the following: 2-GHz bandwidth centered at 2.5 GHz and 22.5° aperture for the brick room; and 1-GHz bandwidth centered at 3.5 GHz and 30° aperture for the cinder block room. We indicate the maximum pixel intensity in certain key areas of each image: the human target and the walls for aperture centered at broadside or the room's corners for aperture centered obliquely.

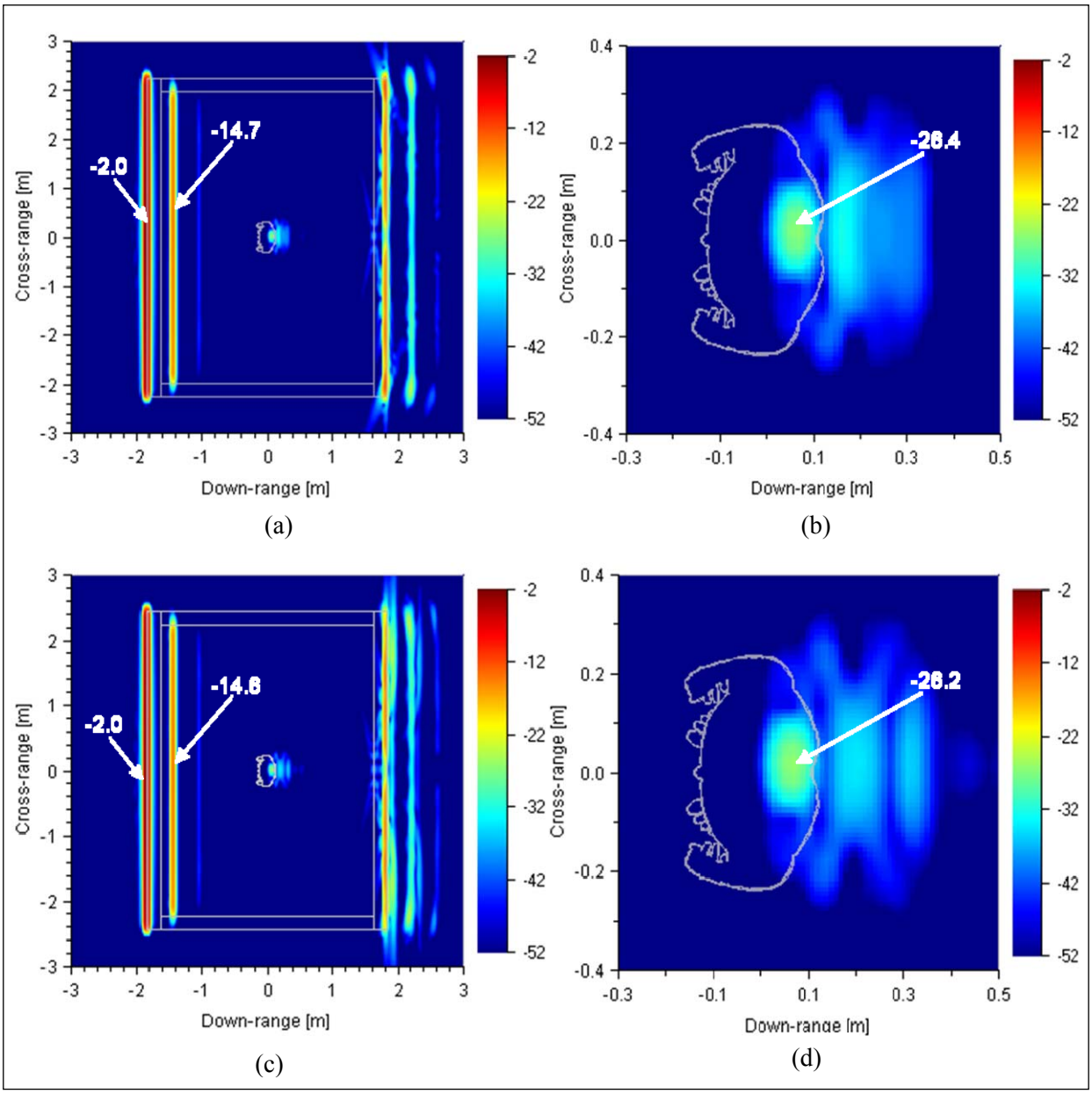

Figure 15. SAR images of a simple room with brick walls, obtained for spotlight mode and the PFA from Xpatch data, 2 GHz bandwidth centered at 2.5 GHz and 22.5° aperture centered at broadside, showing (a) V-V polarization, entire room; (b) V-V polarization, detail around the human; (c) H-H polarization, entire room; and (d) H-H polarization, detail around the human.

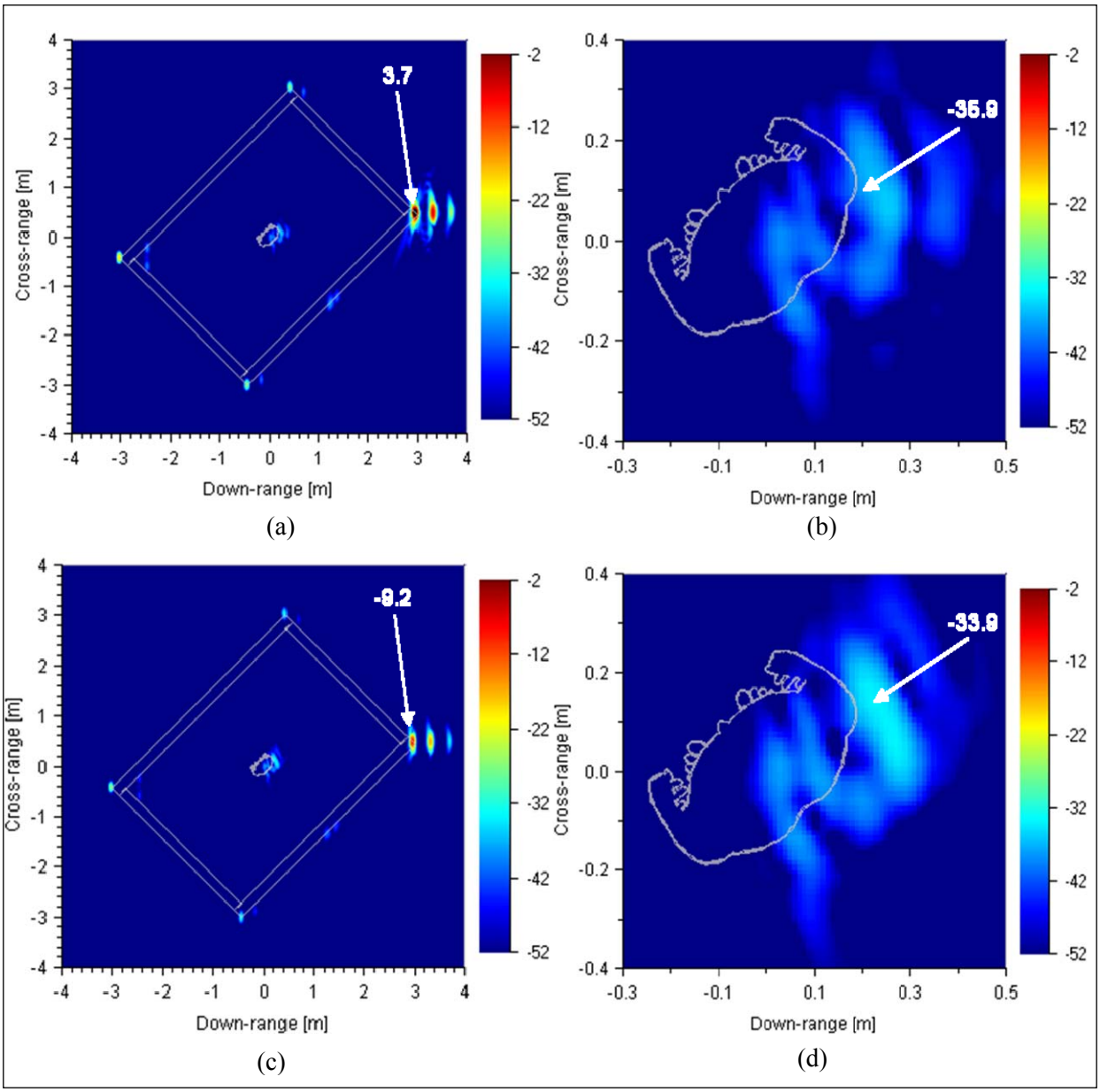

Figure 16. SAR images of a simple room with brick walls, obtained for spotlight mode and the PFA from Xpatch data, 2 GHz bandwidth centered at 2.5 GHz and 22.5° aperture centered at 45°, showing (a) V-V polarization, entire room; (b) V-V polarization, detail around the human; (c) H-H polarization, entire room; and (d) H-H polarization, detail around the human.

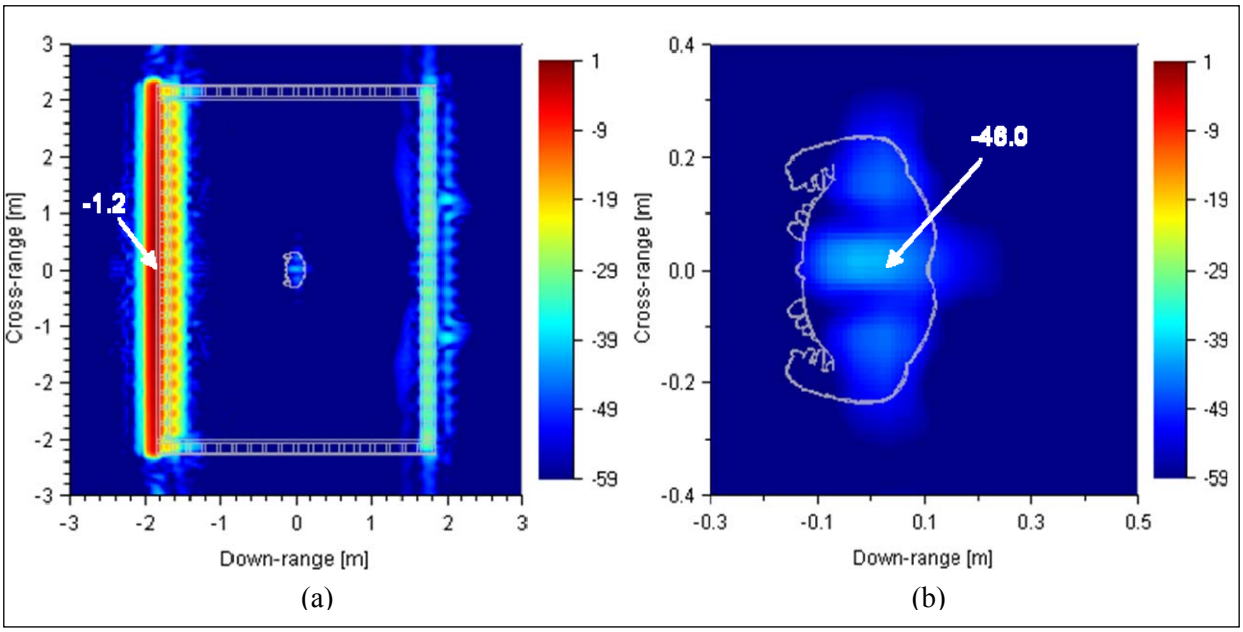

Figure 17. SAR images of a simple room with cinder block walls, obtained for spotlight mode and the PFA from Xpatch data, 1 GHz bandwidth centered at 3.5 GHz and 30° aperture centered at broadside, V-V polarization, showing (a) the entire room and (b) detail around the human.

Comparing various images based on the maximum pixel intensity in specific areas is not always the best way to assess image accuracy. Other image comparison methods could rely on cross-correlations or on analyzing the pixel intensity probability distribution function (PDF) of various image segments. The maximum pixel intensity method is mostly appropriate when applied to targets with simple and regular shapes (such as homogeneous walls), or more generally, when the target shapes obtained by different methods in the image domain are closely correlated (such as the human images obtained in this section by AFDTD and Xpatch). However, when various image formation methods lead to significantly different image shapes of the same target (as we will see in section 3.5), comparing the maximum pixel intensity can produce unreliable outcomes. (Note: The pixel size in the SAR images shown in this report is very small—typically one tenth—compared to the image resolution cell. We achieve this by oversampling and interpolating the radar data during the image formation process. This procedure creates "smooth" pixel maps, free of spurious spikes that could render the maximum pixel intensity comparison ineffective).

The results in this section show a good match between AFDTD and Xpatch for both V-V and H-H polarizations, particularly for the brick wall room (in those cases, the errors are usually below 1 dB). Some significant differences can be noticed at the room corners (especially, the inner/far corners for V-V polarization), where Xpatch overestimates the radar return. This artifact has been discussed elsewhere (*4*) and is due to limited Xpatch accuracy in evaluating scattering by dielectric wedges. Also, by looking at the human images in detail, we can distinguish some discrepancies in the late-time response, which has been explained elsewhere

(*3*). On the other hand, the ghost images are accounted for at the correct locations in all the Xpatch-generated images.

In the case of the cinder block room, we notice fairly clear differences between the AFDTD and Xpatch images. Qualitatively, we notice less reverberation-induced clutter behind the front wall in the Xpatch-generated images. This is expected, given the fact that Xpatch can only account for a limited number of reverberation inside the wall gaps. At the same time, the human signatures behind the cinder block wall computed by the two codes show significant quantitative differences as well.

3.4 The Backprojection Algorithm vs. the Polar Format Algorithm

Another approach to creating SAR images is through the BPA using a strip-map configuration. If the only radar data are available as far-field for a spotlight configuration, we can make a conversion between the two data formats as explained in section 2.2. In this section, we assume that only far-field data sets are available and compare the images obtained through the BPA and PFA. We model the radar signature of the brick room with a human in the middle (figure 4) by Xpatch. For image formation, we use a bandwidth of 2 GHz centered at 2.5 GHz and an effective angular aperture of 30° centered at broadside. The polarization is V-V, with propagation at 0° in elevation. For the BPA, we switch from a circular synthetic aperture to a linear aperture. The linear aperture is placed at a range of 1000 m from the center of the room (which is consistent with the far-field assumption). For each pixel in the image, we add the contribution of all sensor positions within the angular aperture width. In order to create a configuration equivalent to that used in the PFA, the contributions are weighted by a Hanning window (sensors positioned at larger azimuth angles have lower contribution). The excitation spectrum is also weighted by a Hanning window (see figure 3).

The resulting images are shown in figures 18 (PFA) and 19 (BPA). Notice that we use the same image dimensions and the same dynamic ranges (40 dB) in both cases. In this section (as well as in section 3.5), we calibrate the pixel maps such that 0 dB corresponds to the brightest pixel in the image (representing the front side of the front wall). We also mark the pixel intensity in key areas of the image (similar to the previous sections). Notice that the brightest pixels in the human body area do not differ by more than 1 dB between the two imaging methods. Also, the reflection from the back side of the front wall matches within 1 dB. As for the human target, it appears well focused in both images. We conclude this section stating that both algorithms can be used for imaging a room in far-field data collection geometry, with comparable image quality.

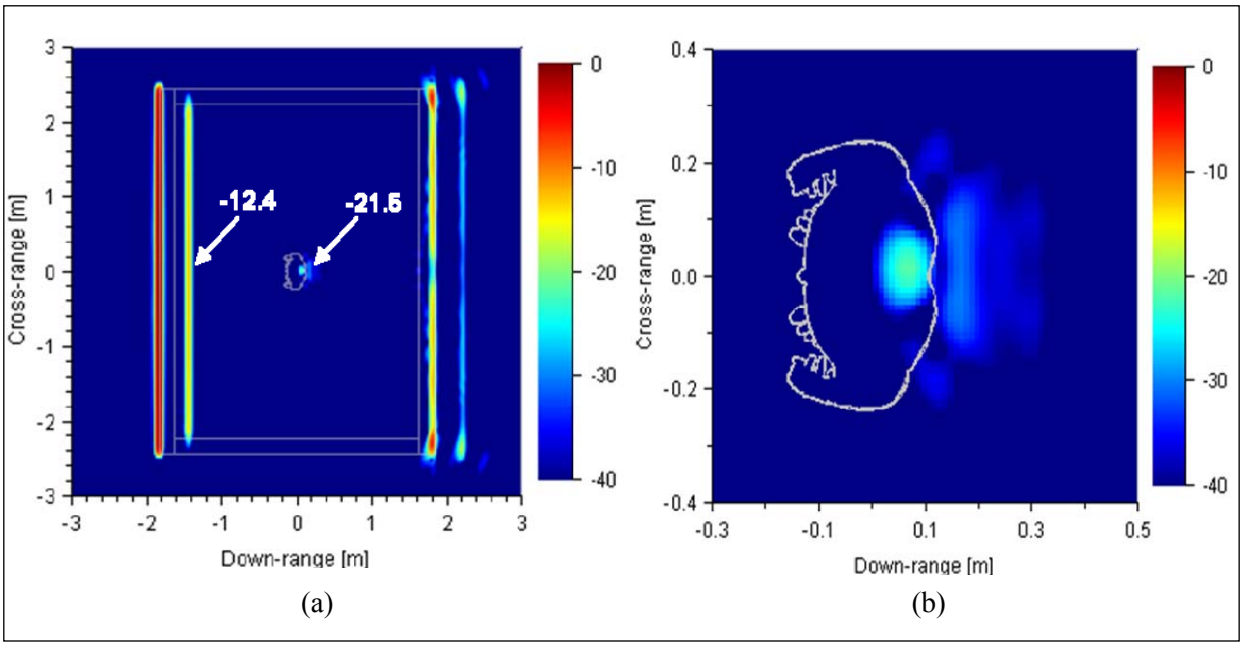

Figure 18. SAR images of a simple room with brick walls, obtained for spotlight mode and the PFA from far-field Xpatch data, 2 GHz bandwidth centered at 2.5 GHz and 30° aperture centered at broadside, V-V polarization, showing (a) the entire room and (b) detail around the human.

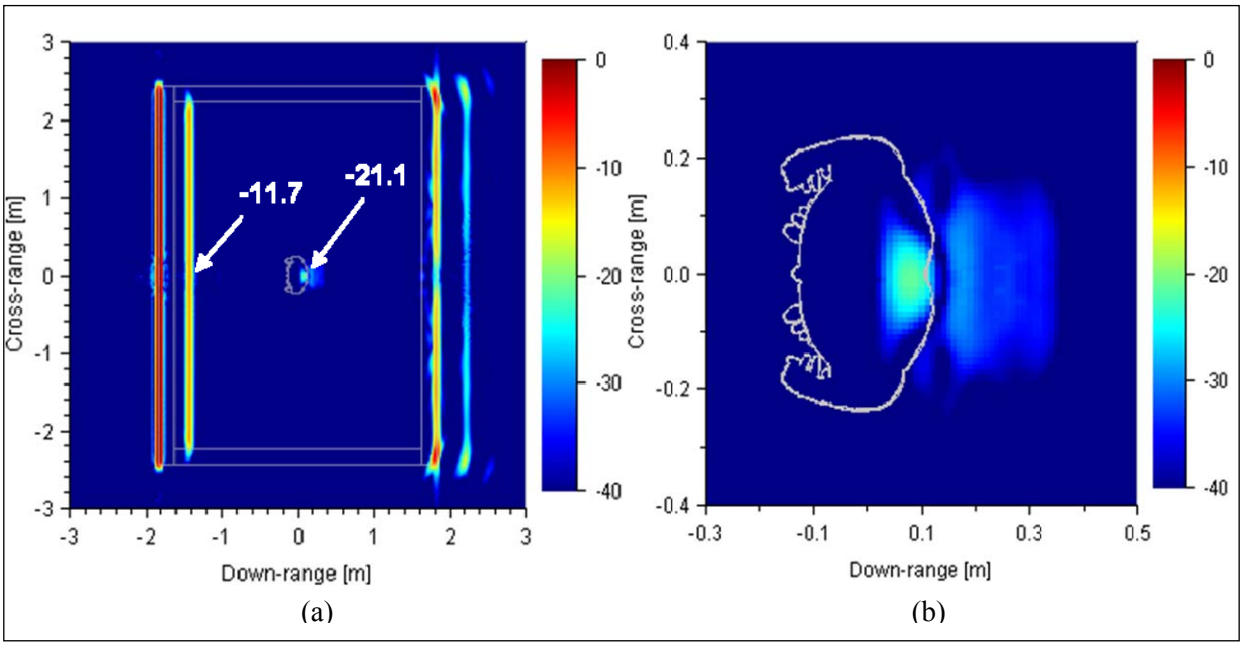

Figure 19. SAR images of a simple room with brick walls, obtained by the BPA from far-field Xpatch data, 2 GHz bandwidth centered at 2.5 GHz and 30° aperture centered at broadside, V-V polarization, showing (a) the entire room and (b) detail around the human.

3.5 The Backprojection Algorithm for Near-Field Geometry

The most realistic imaging scenario involves a near-field data collection along a linear synthetic aperture (strip-map SAR). In this section, we model the radar data for this configuration with Xpatch and apply the BPA for image formation. Again, we apply this scenario to the brick room with a human in the middle (figure 4), with the synthetic aperture parallel to the long side of the building (as shown in figure 1a). The distance from aperture to the center of the room is 11.8 m. The length of the aperture is 15.5 m and the distance between successive sensor positions is 5 cm (that amounts to 311 samples along the aperture). The antenna has a beamwidth of 60° in both elevation and azimuth and always points in the same direction (boresight is perpendicular to the linear synthetic aperture). The antenna phase center is elevated at 1.68 m above the ground. We implemented a Hanning-type spectrum for the excitation waveform, with 2-GHz bandwidth and 2.5 GHz center frequency (same as in the previous section).

Before presenting the imaging results, a more detailed explanation of the way Xpatch implements the near-field radar configuration is necessary (*33, 34*). The antenna is assumed to shoot rays at all angles within the beamwidth, with magnitudes following an angular pattern characteristic to the radiation of the open end of a rectangular waveguide excited by the TE_{10} mode (*35*). The phases of all rays are referenced to the middle of the antenna's aperture. The beamwidth listed in the previous paragraph denotes the 3-dB (or half-power) beamwidth. This type of antenna pattern is fairly representative for practical STTW radar systems. Notice that Xpatch implements the *far-field* pattern of an open waveguide aperture antenna, which is inconsistent with our assumption of the target being in the *near-field* zone. However, given the fact that the very concept of ray tracing assumes far-field propagation, the Xpatch near-field scattering implementation achieves a reasonable compromise within this framework.

The electric field of the TE_{10} mode in the waveguide is assumed to be vertical. This creates an antenna beam with vertical polarization at boresight, but away from that direction; both vertical and horizontal electric fields are present. Therefore, we cannot speak of a pure linear polarization for this type of wide beam antenna (although the vertical polarization is dominant). At the receiver, the PO contributions arriving back to the antenna within the beamwidth are collected after weighting by the same antenna pattern and added coherently. As the end result, Xpatch produces one complex number (magnitude and phase) representing the near-field radar response of the target for each sensor position along the aperture and a given frequency. This response does contain the $1/R$ factor accounting for the radar waves spherical spread.

The SAR image is formed via the BPA. Again, we use the same azimuth angular integration (equal to the antenna beamwidth) for all pixels in the image. In order to achieve this for pixels at the edges of the room in cross-range, the synthetic aperture must extend significantly beyond the room's footprint (recall that the room's cross-range dimension is 5 m, whereas the synthetic aperture length is 15.5 m). For this kind of geometry, given the large antenna beamwidth, some of the incident radar waves penetrate inside the room through the side walls. As in the previous

sections, we introduce a Hanning window angular weighting of the various aperture point contributions. This results in creating an effective aperture of only 30°. An additional feature of the BPA in this scenario is that we do compensate for the spherical spread of the radar waves according to the range from pixel to sensor. Thus, a given target should appear with the same intensity in the image at any downrange (same as for the far-field scenario).

Figure 20 shows the SAR image obtained for the geometry described previously. One difference we immediately notice, as compared to figures 18 and 19, is the double front wall, both for the front and back side. A similar effect is seen for the back wall. This is explained by the presence of the ground plane, which forms a perfect corner with the front wall. Since the rays bounced by the ground and wall travel a longer path than the rays reflected directly by the wall, they show up in the image as a delayed version of the front wall. This is an important effect for any imaging system that looks at a depression angle, when the targets form perfect corners with the ground.

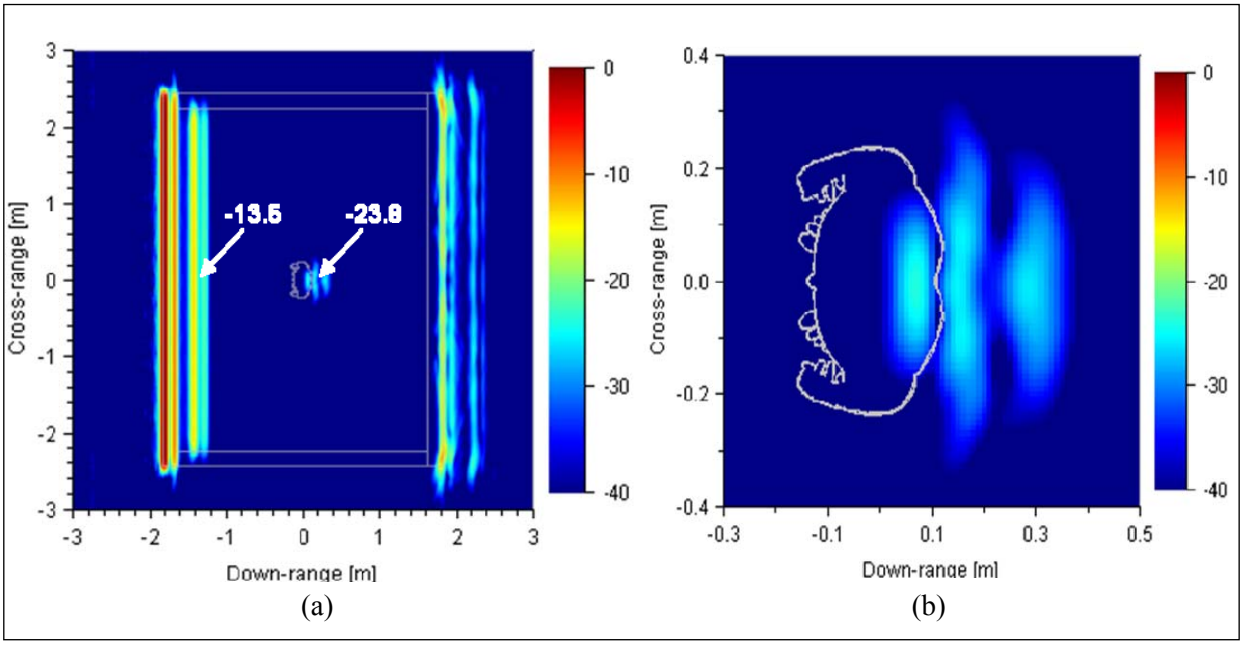

Figure 20. SAR images of a simple room with brick walls, obtained for strip-map mode and the BPA from near-field Xpatch data, 2 GHz bandwidth centered at 2.5 GHz and 30°effective integration angle, V-V polarization, showing (a) the entire room and (b) detail around the human.

Note: the computational mesh includes a ground plane in this case.

To better illustrate the difference between various propagation paths, we represented them schematically in figure 21. The only rays that contribute to the first (brightest) image of the front side of the front wall are those shot perpendicular to the wall (both in azimuth and elevation). The replica that we see immediately behind this front side image represents the rays that bounce off the ground-wall inner corner. The range of this delayed version of the wall's front side to the aperture equals the distance from the antenna to the wall's bottom edge. Again, only rays perpendicular to the wall in azimuth are received in the backscatter direction. Similar

considerations can be applied to the image of the human target. By comparing the image area around the human (figures 18b, 19b, and 20b), we notice significant differences in the image shapes obtained by the three procedures, in the sense that the near-field image (figure 20b) appears smeared, both in downrange and cross-range. We attribute this smearing to the ground bounce effect explained previously, with the difference that, in this case, rays in all azimuth directions contribute to backscatter (hence, the image extension in cross-range).

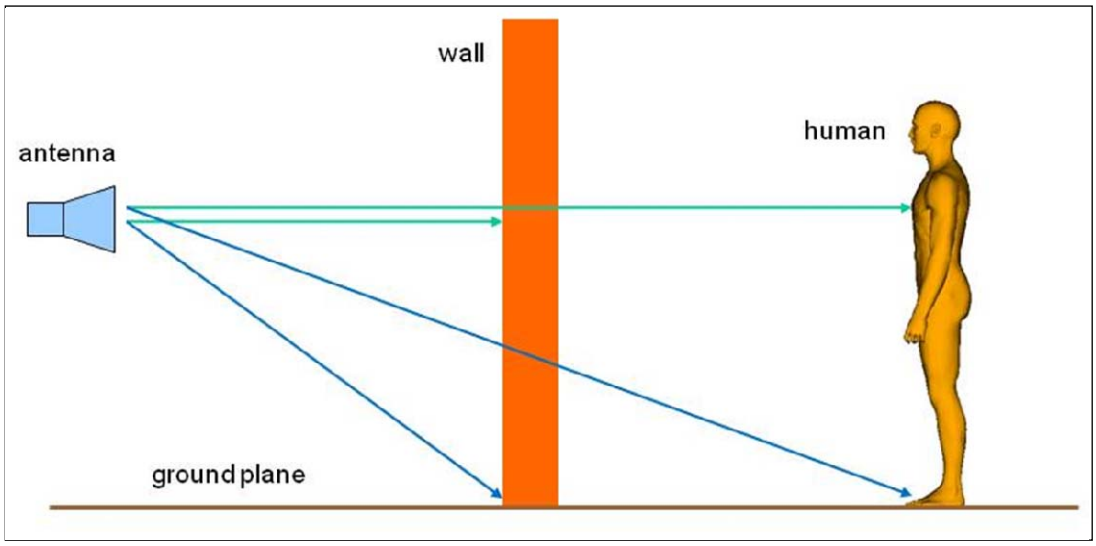

Figure 21. Diagram illustrating the effect of the ground plane on the near-field SAR image. The difference in length between the green (direct) and blue (ground-bounced) propagation paths creates double images for the wall and the human.

In figure 22, we present the room image obtained by the same method, but with the ground plane removed. (Note: In this scenario we completely remove the room's ceiling and floor.) We can clearly see that the "double wall" image is greatly suppressed in this case, although it does not completely disappear. In this case, the contribution to the delayed version of the wall image comes from diffraction off the wall's top and bottom edges. It is interesting that this diffraction contribution appears in the image at the same range as the ground bounce in figure 20, since the propagation delay is the same in the two cases. The difference in magnitude between the two cases is illustrative of the difference in backscattering from an inner corner versus an outer corner (*19*).

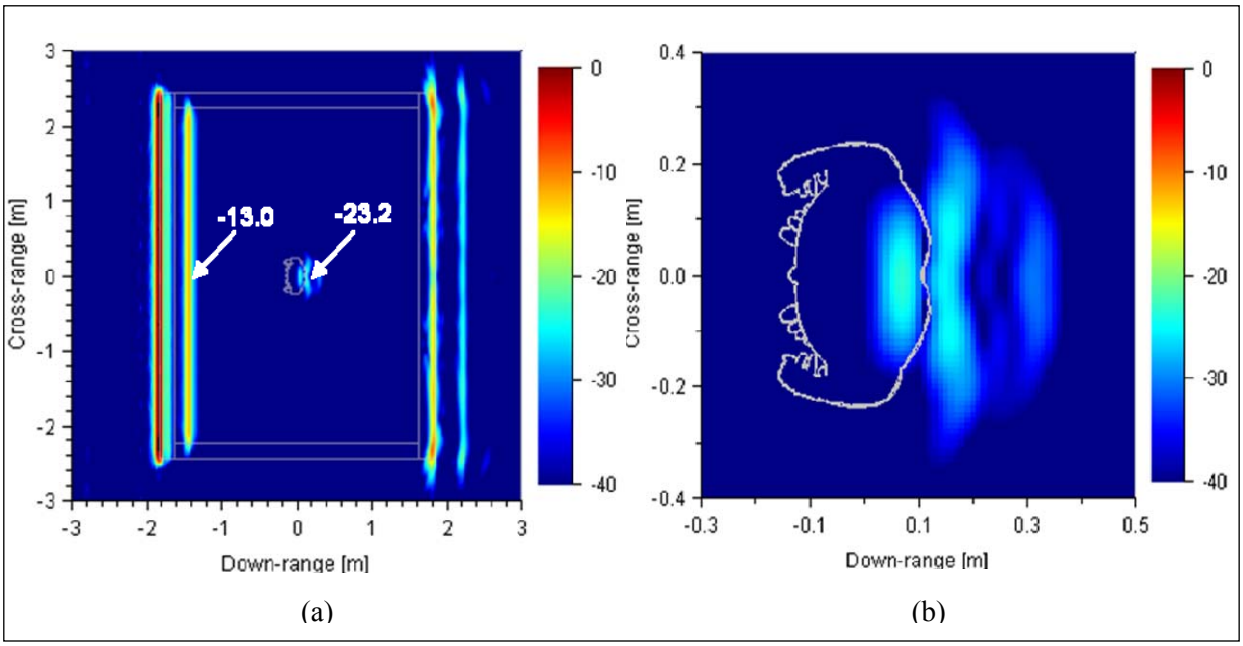

Figure 22. SAR images of a simple room with brick walls, obtained for strip-map mode and the BPA from near-field Xpatch data, 2 GHz bandwidth centered at 2.5 GHz and 30°effective integration angle, V-V polarization, showing (a) the entire room and (b) detail around the human.

Note: the computational mesh does not include a ground plane in this case.

It is interesting that, because of imperfections in the ground and front wall forming a perfect 90° corner, the ground bounce effect in an actual STTW imaging scenario may not be as severe as seen in figure 20 (*9*). Also, since field-measured SAR images most likely display a larger amount of clutter, as well as possibly lower resolution than the simulated images, many of the fine features of the human image described in this section may be completely obscured in a real-life scenario.

By comparing the images in figure 22 with those in figures 18 and 19, we notice that the relative magnitudes of the back side of the front wall, as well as the brightest pixel in the human area agree reasonably well (within 2 dB) across the imaging methods. When we add the ground plane (figure 21), we notice that the differences increase by another 0.5 dB. The shadow cast by the human on the back wall is present in all images. We should also mention that, in general, we expect near-field radar images to appear noisier than those obtained for far-field geometries. This fact is difficult to demonstrate using a simple example such as the room considered in this report, but is consistent with our experience on imaging more complex buildings (*9*).

3.6 Exploiting Cross-polarization to Image a Human in a Room

At typical operational frequencies for STTW radar (1–3 GHz), the round-trip attenuation through walls can be considerable, varying between 20 dB for brick and 40 dB for concrete (for a 0.2-m-thick wall) (*32*). Therefore, an imaging radar would need a large dynamic range in order to detect human targets behind such walls, since the front wall always appears much brighter

than the target. One possible solution that could eliminate the walls from the image (suggested in section 3.1) would be to use an imaging geometry at an oblique angle. Another way to achieve that would be to operate the radar in cross-polarization. This method would also attenuate the images of objects with certain geometric characteristics, while emphasizing the human targets. This idea is based on the following observations on polarimetric scattering phenomenology:

- Reflection from the wall surface (planar interface) does not change the incident polarization; therefore, the cross-polarized reflected wave is null (regardless of the incidence angle).
- Edge diffraction does not produce cross-polarized fields in the backscatter as long as the edge projection onto a plane perpendicular to the incident wave propagation vector is aligned to either the vertical or horizontal electric field vector. If we assume plane waves propagating at 0° elevation, then this is always the case for both the vertical and horizontal wall edges, regardless of the azimuth incident angle.
- The room vertices may produce cross-polarized fields in the backscatter, but their contribution to the SAR image is a higher-order effect.
- The off-broadside scattering from the human body has a measurable cross-polarization component, due to the body's irregular shape.

To verify these theoretical observations, we obtained the vertical-horizontal (V-H) polarized SAR images of the room in figure 4. The simulations were performed with AFDTD, since Xpatch does not provide good accuracy for cross-polarization computations. The imaging configuration was the spotlight SAR using the PFA, with the same parameters as in sections 3.1 and 3.2. The results are shown in figure 23, for the brick room at broadside incidence (a), the brick room at oblique incidence (b), and the cinder block room at broadside incidence (c).

The SAR images in figure 23 demonstrate very good rejection of the walls—the only features left in the images are the human and its ghost image projected onto the back wall(s). We can also distinguish the inside corner in figure 23b, but at much lower intensity relative to the human as compared to figure 9. Notice though that the cross-polarization return from targets inside the room is very weak in absolute terms, since the radar waves are still subject to the same through-wall propagation losses. Thus, the intensity of the cross-polarization human images is ~20 dB (for the brick walls) to 30 dB (for the cinder block walls) lower than the ones for the co-polarization images. Note that the intensity scales in figure 23 are 40 to 50 dB lower than those for the previous cases. With such low-level signals, the radar performance may be limited by noise.

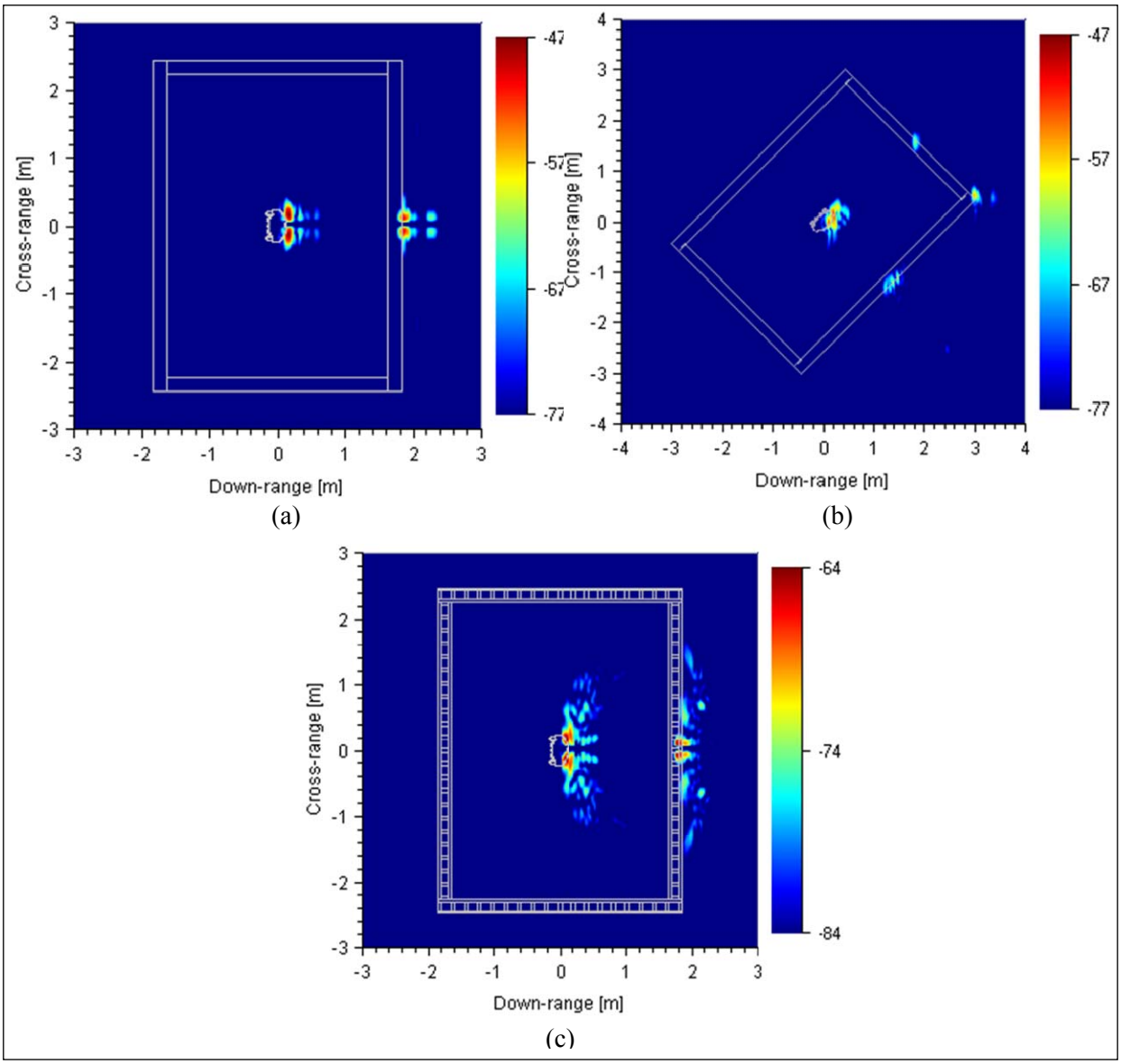

Figure 23. SAR images of a simple room, obtained for spotlight mode and the PFA from AFDTD data in cross-polarization (V-H), 2 GHz bandwidth centered at 2.5 GHz and 22.5° aperture, showing (a) brick room at broadside view, (b) brick room at 45° view, and (c) cinder block walls at broadside view.

Note: For the cinder block case, the aperture size is 30°.

It is interesting to predict what would happen in the case when the incident wave propagation vector is not directed at 0° elevation. For a radar system placed in the far-field, that would correspond to an airborne-based scenario. However, this case could also be relevant for a ground-based radar placed in the near-field, where the incident beam hits the wall edges at oblique elevation angles (as explained in section 3.5). In that situation, the horizontal wall edges project at an oblique angle onto a plane perpendicular to the direction of propagation and create cross-polarized scattered field. Nevertheless, since most of the cross-polarized energy diffracted by these edges scatters forward and only very little in backscatter, this effect should not have a

significant impact on the SAR image. In fact, only discontinuities along the horizontal edges should appear in the cross-polarization SAR images. Also, we expect this effect to be stronger as the elevation angle increases.

An important practical issue in obtaining cross-polarized SAR images with UWB STTW radar systems is the fact that typical wide-beam antennas (such as horn antennas) used by such systems do not display a pure polarization (either vertical or horizontal) away from boresight (*35*). That means it would not be possible to obtain pure cross-polarization signatures of targets at oblique azimuth angles using these antennas. Note that this would not be an issue for higher frequency SAR systems, where small integration angles about boresight are required, so the pure polarization assumption is mostly valid. An additional complication to this scenario may be introduced by the fact that, in many practical cases, the location of the (separate) transmitting and receiving antennas creates a slightly bistatic configuration that could increase the cross-polarization contamination upon wall reflection. A possible solution to this problem is to perform a polarimetric calibration of the radar by introducing a post-processing compensation procedure (*36*). Another possible approach would involve using UWB, wide-beam antennas with good cross-polarization isolation, such as the Vivaldi slot (*37*) or the log-periodic (*35*) antenna.

3.7 The Human and a Metallic Cabinet Placed in a Simple Room

In this section, we consider the scenario described in figure 6, where a human and a metallic cabinet are placed together in a simple room. Our goal is to determine if we can discriminate between the two types of objects based on the SAR images. These images were obtained for both co-polarization (V-V) and cross-polarization (V-H) and are shown in figures 24 (brick walls) and 25 (cinder block walls). For the brick room, the bandwidth is 2 GHz centered at 2.5 GHz and the aperture is 22.5° centered at broadside. For the cinder block room, we use the same frequencies, but the aperture is 30° centered at broadside. The EM modeling and image formation methods are identical to those in section 3.1.

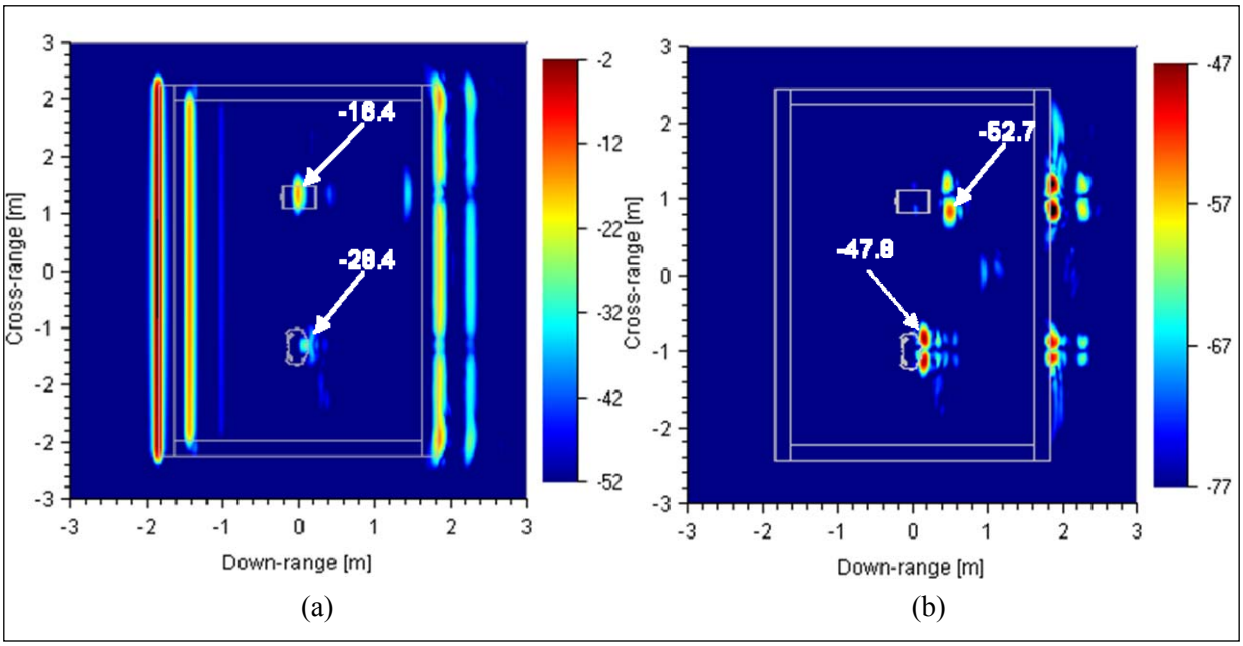

Figure 24. SAR images of a simple room with brick walls, containing a human and a cabinet, obtained for spotlight mode and the PFA from AFDTD data, 2 GHz bandwidth centered at 2.5 GHz and 22.5° aperture centered at broadside, showing (a) V-V polarization and (b) V-H polarization.

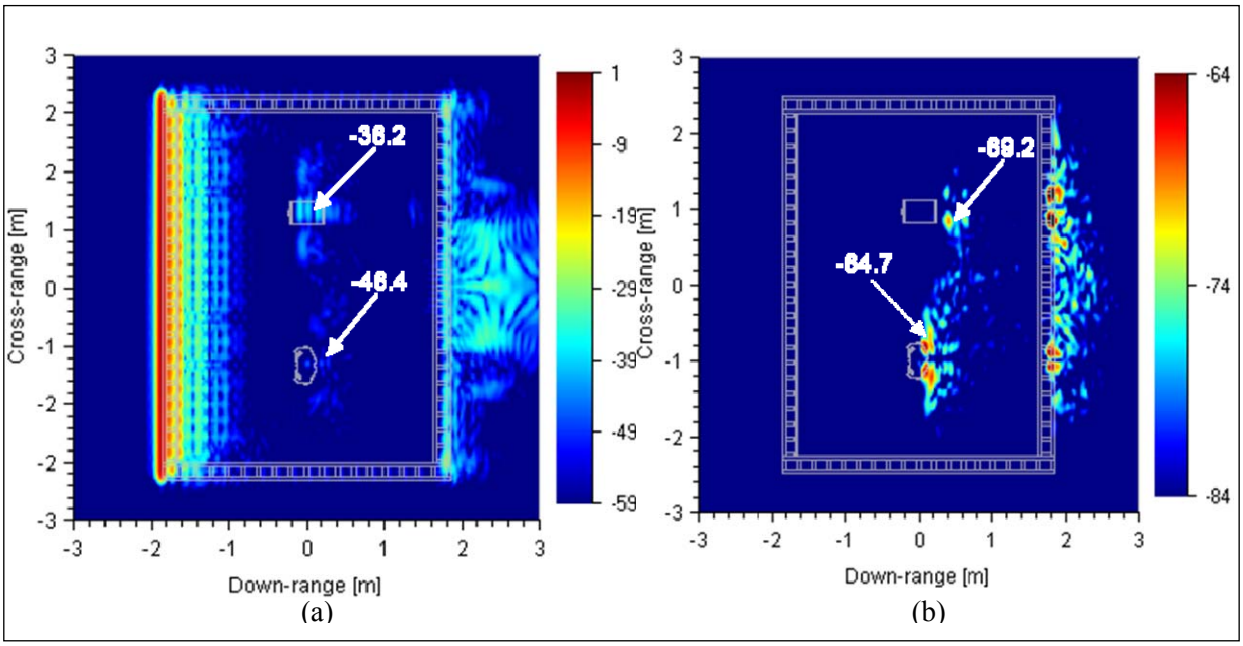

Figure 25. SAR images of a simple room with cinder block walls, containing a human and a cabinet, obtained for spotlight mode and the PFA from AFDTD data, 2 GHz bandwidth centered at 2.5 GHz and 30° aperture centered at broadside, showing (a) V-V polarization and (b) V-H polarization.

As expected, the metallic cabinet appears brighter than the human in co-polarization for both wall material types. Thus, for the brick wall (figure 24a), the cabinet image peaks at –16.4 dB, whereas the human image peaks at –28.4 dB. For the cinder block wall (figure 25a), the cabinet

image peaks at –36.2 dB, whereas the human image peaks at –46.4 dB. We can also see noticeable differences between the image shapes of the cabinet and the human, especially for the brick wall room. Moreover, we expect the orientation angle dependence of these images to be significantly different.

However, in the cross-polarization images, we notice that the human appears brighter than the cabinet. Thus, for the brick room (figure 24b), the human peaks at –47.8 dB, whereas the cabinet peaks at –52.7 dB. For the cinder block wall (figure 25b), the human peaks at –64.7 dB, whereas the cabinet peaks at –69.2 dB. The explanation is that the cabinet looks like a rectangular box with flat surfaces and straight edges, which are all perpendicular to each other, and, as discussed in section 3.6, the cross-polarization backscatter return from such objects is expected to be very low. On the other hand, the human displays more curved and irregular surfaces, which generally produce a larger cross-polarization return. This suggests that operating the radar in cross-polarization not only allows significant rejection of the walls in the SAR image, but also de-emphasizes objects with flat-surface, straight-edge type of geometry (as many furniture objects conform to this type of model). Finally, we notice that ghost images of both targets are present in all the SAR images shown in figures 24 and 25, and that, interestingly, in the cross-polarization case, the cabinet ghost images appear brighter than the human ghost images (they also appear brighter than the targets themselves).

4. Conclusions

Building structure imaging and behind-the-wall target detection based on radar images are key components of the Army and Department of Defense (DoD) efforts in developing STTW capabilities. In this report, we performed a detailed phenomenological investigation of STTW SAR imaging systems based on computer simulations. These results are important in helping the radar engineers predict system performance, choose optimal design parameters, develop imaging algorithms, as well as understand and mitigate image artifacts and other subtle propagation and scattering effects.

Essential to our analysis is the ability to separate various sources of errors or artifacts in the SAR images. Thus, based the simulations presented in this report, we can distinguish three types of image errors: (1) image artifacts created by EM phenomenology, (2) errors in the EM modeling codes, and (3) errors introduced by the image formation methods. In the first category, the delays were caused by propagation through walls, which misplace and defocus the targets in the SAR image, and by the multipath propagation and scattering, which introduce ghosts or unwanted clutter in the image. Certain imaging techniques can mitigate these issues (*23–26*); however, they were outside the scope of this work. We discussed the second type of errors by comparing results obtained with different EM simulation techniques. We also analyzed issues related to the image formation processes: limited resolution, sidelobes, grating lobes, interpolation in the PFA, and

windowing. We showed that, by carefully applying standard EM modeling techniques and image formation algorithms, one can eliminate or keep under control the errors in the second and third categories. That is a key step in enabling the correct interpretation of SAR images and understanding the underlying EM phenomenology.

A separate type of error that was not discussed in this report was introduced by the radar measurement. These errors may include radar system noise, uncompensated positioning errors, and other effects that are dependent on the particular radar system implementation (*11, 12*). Our preliminary understanding of the relatively error-free SAR images obtained via computer modeling greatly enhanced our ability to interpret the much more complex radar images obtained in a real-life STTW environment.

In terms of EM modeling, we used the AFDTD code to obtain "exact" radar signature solutions, as well as validated the solutions generated by Xpatch, which is an approximate solver. This validation work continues our study in reference 4 by comparing pixel intensity values of key features in the SAR images. Our conclusion is that the two methods produce very similar results, with some notable differences at the inner corners of a room as well as in the case of imaging a room with cinder block walls.

Most of our SAR images were created by the PFA in combination with a far-field, spotlight geometry, which is not a very realistic configuration for practical STTW radar imaging systems. In order to validate the results obtained by this approach, we compared them with more realistic imaging geometries and algorithms, such as the BPA combined with the strip-map configuration in the far-field and the near-field. We noticed that most image features do not depend much on the imaging technique. However, the images obtained for far-field geometries tended to be less noisy than those produced by near-field geometries. Particularly, the ground plane effects can be significant for a near-field antenna with a wide beam in elevation, whereas the far-field simulations (which assume propagation at 0° elevation) do not include these effects. These results are important in interpreting SAR images obtained both via simulations or real measurements.

The room imaging examples in this report focused on a simple four-wall room with a human (and, in some examples, a file cabinet) placed inside. We looked at various building materials (brick, concrete, and cinder block) and noticed the image differences induced both by the wall propagation loss and the wall geometrical structure. As expected, the uniform walls produced clean images; however, for solid concrete walls, the round-trip attenuation was very severe, making behind-the-wall target detection at the frequencies considered here a challenging task. This type of walls may require lower radar frequencies of operation, such as those in the very high frequency (VHF) or ultra high frequency (UHF) bands. The cinder block structures produced a large amount of clutter directly behind the wall, in an area where target detection would again be problematic. Also, we noticed a de-focusing of the target in the cinder block wall case, which we attributed to the multiple possible propagation paths and delays of the radar

waves reaching the target. In all cases, we noticed the presence of ghost images of the target on the back wall(s)—this phenomenon is a consequence of multipath propagation inside a room and is explained in detail in the appendix.

Another interesting technique that we analyzed in this work was imaging a room using cross-polarization. We demonstrated that, when using this mode, the walls practically disappear from the image, whereas the human targets still display a sizeable signature relative to the image background. Moreover, when we introduced furniture objects with regular rectangular shapes (such as a file cabinet), their signature was significantly lower in the cross-polarization image. As pointed out in section 3.6, there are important practical issues in implementing an actual radar system that produces through-the-wall cross-polarization data. Nevertheless, this is an interesting concept that deserves more investigation. As shown in reference 38, the cross-polarization mode may also yield features that allow detection of small weapons in a STTW environment.

In a follow-up to this report, we will present simulated images of a larger, more complex room, containing multiple people, furniture objects, and internal walls. The scenario could be further complicated by the presence of plumbing, wiring, and heating-ventilation-air-conditioning systems. We will also compare images obtained from real measurements of a large building with those modelled by Xpatch. As a future concept, we believe that three-dimensional building imaging would represent a great improvement in attempting to resolve targets inside a building, especially when multiple floors are involved. However, this approach would require very large amounts of data to be collected (via measurements or simulations) and processed (most likely via the BPA).

5. References

1. Dogaru, T.; Nguyen, L.; Le, C. *Computer Models of the Human Body Signature for Sensing Through the Wall Radar Applications*; ARL-TR-4290; U.S. Army Research Laboratory: Adelphi, MD, September 2007.

2. Le, C.; Dogaru, T. *Numerical Modeling of the Airborne Radar Signature of Dismount Personnel in the UHF-, L-, Ku-, and Ka-Bands*; ARL-TR-4336; U.S. Army Research Laboratory: Adelphi, MD, December 2008.

3. Dogaru, T.; Le, C. *Validation of Xpatch Computer Models for Human Body Radar Signature*; ARL-TR-4403; U.S. Army Research Laboratory: Adelphi, MD, March 2008.

4. Dogaru, T.; Le, C. *Simulated Radar Range Profiles of Simple Room as Computed by FDTD and Xpatch*; ARL-TR-4420; U.S. Army Research Laboratory: Adelphi, MD, April 2008.

5. Innocenti, R. Sparse array of RF sensors for sensing through the wall. *Proceedings of SPIE* **2007**, *6547*.

6. Dogaru, T.; Le, C.; Kirose, G. *Time-Frequency Analysis of a Moving Human Doppler Signature*; ARL-TR-4728; U.S. Army Research Laboratory: Adelphi, MD, February 2009.

7. Martone, A.; Innocenti, R.; Ranney, K. *Moving Target Indication for Transparent Urban Structures*; ARL-TR-4809; U.S. Army Research Laboratory: Adelphi, MD, May 2009.

8. Nguyen, L.; Ressler, M.; Sichina, J. Sensing Through the Wall Imaging Using the Army Research Lab Ultra-wideband Synchronous Impulse Reconstruction (UWB SIRE) Radar. *Proceedings of SPIE* **2008**, *6947*.

9. Le, C.; Dogaru, T.; Nguyen, L.; Ressler, M. Ultra-wideband (UWB) Radar Imaging of Building Interiors: Measurements and Predictions. *IEEE Transaction on Geophysics and Remote Sensing* **May 2009**, *47*, 1409-1420.

10. Soumekh, M. *Synthetic Aperture Radar Signal Processing*; Wiley: New York, 1999.

11. Carrara, W.; Goodman, R.; Majewski, R. *Spotlight Synthetic Aperture Radar – Signal Processing Algorithms*; Artech House: Boston, MA, 1995.

12. Jakowatz, C.; Wahl, D.; Eichel P.; Ghiglia, D.; Thompson, P. *Spotlight-Mode Synthetic Aperture Radar: A Signal Processing Approach*; Kluwer Academic Publishers: Norwell, MA, 1996.

13. Dogaru, T. *AFDTD User's Manual*; ARL-TR-5145; U.S. Army Research Laboratory: Adelphi, MD, March 2010.

14. Taflove, A.; Hagness, S. C. *Computational Electrodynamics: The Finite-Difference Time-Domain*; Artech House, Boston, MA, 2000.

15. Ruch, G.; Barrick, D. E.; Stuart, W. D.; Krichbaum, C. K. *Radar Cross Section Handbook*; Plenum Press: New York, 1970.

16. Chamma, W. *EM Modelling of a Realistic Room for Through-the-Wall Radar Applications*; Technical Memorandum TM 2007-022; Defence Research and Development Canada: Ottawa, Canada, January 2007.

17. Clark, B. Trial Results of a Stand-off Sense-Through-The-Wall Radar. *Proceedings of the 55th Annual MSS Tri-Service Radar Symposium,* June 2009.

18. Hunt, A. R. Use of a Frequency-hopping Radar for Imaging and Motion Detection Through Walls. *IEEE Transaction on Geophysics and Remote Sensing* **May 2009**, *47*, 1402–1408.

19. Balanis, C. *Advanced Engineering Electromagnetics*; Wiley: New York, 1989.

20. Knittle, C.; Doren, N.; Jakowatz, C. *A Comparison of Spotlight Synthetic Aperture Radar Image Formation Techniques*; Sandia Report SAND96-2460 UC-900; Sandia National Laboratories: Albuquerque, NM, October 1996.

21. Oppenheim, A. V.; Schafer, R. W. *Discrete-time Signal Processing*; Prentice Hall: Englewood Cliffs, NJ, 1989.

22. Shaeffer, J. F.; Hom, K. W.; Baucke, R. C.; Cooper, B. A.; Talcott, N. A. *Bistatic k-space Imaging for Electromagnetic Prediction Codes for Scattering and Antennas*; Technical Paper NASA-TP-3569; National Aeronautics and Space Administration: Langley, VA, July 1996.27.

23. Ahmad, F.; Amin, M. G. Multi-location Wideband Synthetic Aperture Imaging for Urban Sensing Applications. *Journal of the Franklin Institute* **September 2008**, *345*, 618–639.

24. Khatri, H.; Le, C. Estimation of Electromagnetic Parameters and Thickness of a Wall Using Synthetic Aperture Radar. *Proceedings of SPIE* **2007**, *6547*.

25. Ahmad, F.; Amin, M. G.; Mandapati, G. Autofocusing of Through-the-Wall Radar Imagery Under Unknown Wall Characteristics. *IEEE Transactions on Image Processing* **July 2006**, *16*, 1785–1795.

26. Wang, G.; Amin, M .G. Imaging Through Unknown Walls Using Different Standoff Distances. *IEEE Transactions on Signal Processing* **October 2006**, *54*, 4015–4025.

27. Pena, D.; Feick, R.; Hristov, H.; Groto, W. Measurement and Modeling of Propagation Losses in Brick and Concrete Walls for the 900-MHz Band. *IEEE Transactions on Antennas and Propagation* **January 2003**, *51*, 31–39.

28. Muqaibel, A.; Safaai-Jazi, A.; Bayram, A.; Attiya, A.; Riad, S. Ultra-wideband Through-the-Wall Propagation. *IEE Proceedings – Microwave, Antennas and Propagation* **December 2005**, *152*, 581–588.

29. Stone, W. *Electromagnetic Signal Attenuation in Construction Materials*; NISTIR 6055; National Institute of Standards and Technology: Gaithersburg, MD, October 1997.

30. Yang, C. F.; Ko, C. J.; Wu, B. C. A Free Space Approach for Extracting the Equivalent Dielectric Constants of the Walls in Buildings. *1996 IEEE Antennas and Propagation International Symposium*, Baltimore, MD, July 1996, 1036–1039.

31. ARL MSRC Web page. http://www.arl.hpc.mil (accessed August 2009).

32. Farwell, M.; Ross, J.; Luttrell, R.; Cohen, D.; Chin, W.; Dogaru, T. Sense Through the Wall System Development and Design Considerations. *Journal of the Franklin Institute* **September 2008**, *345*, 570–591.

33. Yu, C. L.; Kipp, R.; Andersh, D. J.; Lee, S. W. Near-field Electromagnetic Modeling and Analysis. *1997 IEEE Antennas Propagation International Symposium* **July 1997**, *2*, 1168–1171.

34. Jeng, S. Near-field Scattering by Physical Theory of Diffraction And Shooting and Bouncing Rays. *IEEE Transactions on Antennas and Propagation* **April 1998**, *46*, 551–558.

35. Balanis, C. *Antenna Analysis and Design*; Wiley: New York, 2002.

36. Barnes, R. M. *Polarimetric Calibration Using In-scene Reflectors*; MIT Lincoln Laboratory Project Report TT-63: Lexington, MA, September 1986.

37. Langley, J.D.S.; Hall, P. S.; Newham, P. Novel Ultrawide-bandwidth Vivaldi Antenna with Low Crosspolarisation. *IEE Electronics Letters* **November 1993**, *29*, 2004–2005.

38. Dogaru, T.; Le, C. *Through-the-Wall Small Weapon Detection Based on Polarimetric Radar Techniques*; ARL-TR-5041; U.S. Army Research Laboratory: Adelphi, MD, December 2009.

INTENTIONALLY LEFT BLANK.

Appendix. Ghost Image Analysis

The problems of multiple scattering and multipath propagation have received a great deal of investigation, especially in the context of wireless propagation within a building environment. Our interest here is in obtaining SAR images of objects placed in such an environment. It is interesting that the process of creating SAR images based on UWB and wide-angle radar data seems to mitigate the multipath propagation effects in most cases, since the paths involving multiple scattering have different phases at different frequencies and angles (thus, they do not add coherently at a given image point). However, as we have already seen in this report, multipath propagation and scattering can create significant artifacts in SAR images. The ground bounce (section 3.5) and cinder block wall reverberation (section 3.2) represent clear examples where these phenomena impact the radar images. As we show in this appendix, when a target is placed in a room, ghost images form at points where multiple scattering paths add coherently. We would like to emphasize that this is not a trivial effect in SAR imaging, and it is specific to the STTW environment.

In order to illustrate this effect (figure A-1), we consider a small target (*H*) placed in a four-wall room in an arbitrary position and perform a simple ray tracing scenario for an arbitrary incidence angle α. For clarity, we choose an oblique incidence angle (the broadside incidence case will be discussed later). To simplify the analysis, we neglect the propagation delays through the walls. Since the target diffracts fields in all directions, we can trace the diffracted rays that reflect from the back wall and return in the backscatter direction. According to the image theory (*19*), the rays reflected from the back wall (at point *B*) appear to emanate from an image source placed in *I* (the point symmetric to *H* with respect to the back wall). If we schematically represent the target contribution to the radar range profile at this incidence angle (shown at the bottom of figure A-1), we obtain a direct return from the target (the first peak) and the reflection from the back wall (the second peak). Let *P* be the projection of *H* onto the back wall. From simple geometric considerations, the distance between the two peaks equals *d*, which is the projection of the *HP* segment onto the direction of incidence. Now consider the contributions of the back wall reflection for various angles of incidence. It is clear that, for any incidence angle, the secondary peaks in the range profiles always back-project to the point *P*. Therefore, all the secondary peaks add coherently at point *P*, which will appear with significant brightness in the SAR image and create the ghost image.

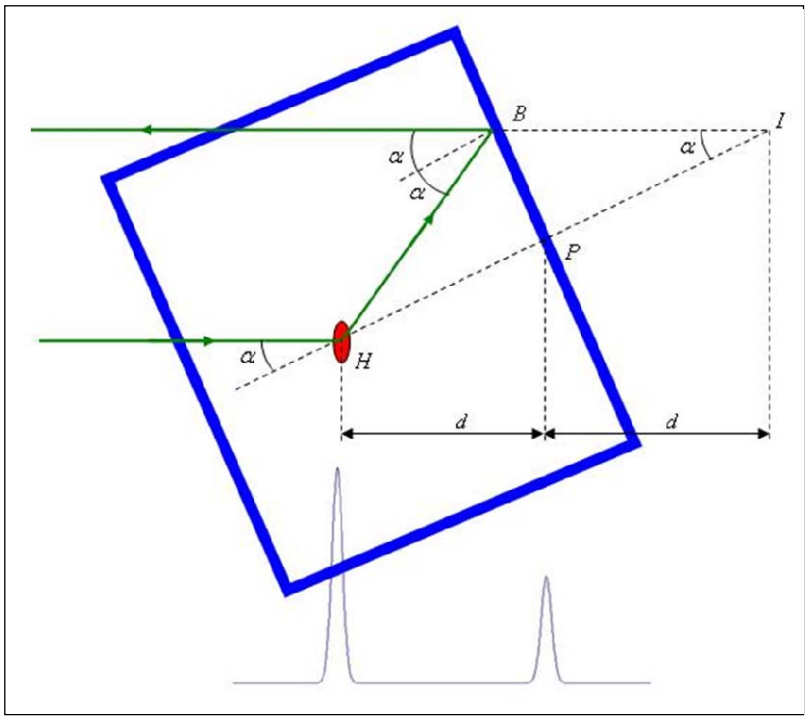

Figure A-1. Diagram explaining the origin of the ghost image of an object placed in a room. This ray tracing example considers one arbitrary angle of incidence. The target contribution to the radar range profile (obtained in backscatter) is shown in blue at the bottom of the picture.

It can also be shown that, in certain cases, the same target may produce ghost images along both back walls. This situation is illustrated in figure A-2. Generally, we need a larger incidence angle in order to observe false images along both back walls. With reference to figure A-2, the condition to observe two ghost images is

$$\tan\alpha > \frac{a}{b} \tag{A-1}$$

It is interesting to mention that repeated reflections between the target and the back wall(s) can produce additional ghost images, which appear further from the back wall(s) in the SAR images. To demonstrate this, we plotted again the images obtained in section 3.6, for cross-polarization, with an extended image space. As one can see in figure A-3a, further replicas of the ghost image appear behind the back wall at regular intervals equal to the distance between the human and the back wall. Even more interestingly, when we consider an aperture centered obliquely (figure A-3b), we notice a large number of additional ghost images that form a rectangular grid. Although these additional ghost images could confuse a target detection algorithm based on SAR images, they should be relatively easy to dismiss based on the facts that (a) their intensity decreases with each additional reflection and (b) they appear outside the footprint of the room or building.

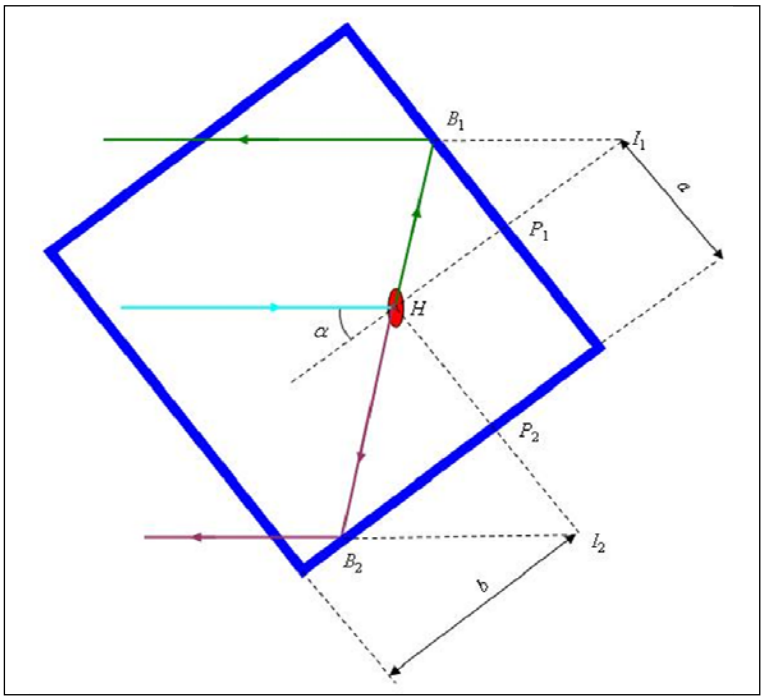

Figure A-2. Diagram showing the formation of two ghost images of an object placed in a room. The ghost images appear along the two back walls when inequality (8) holds.

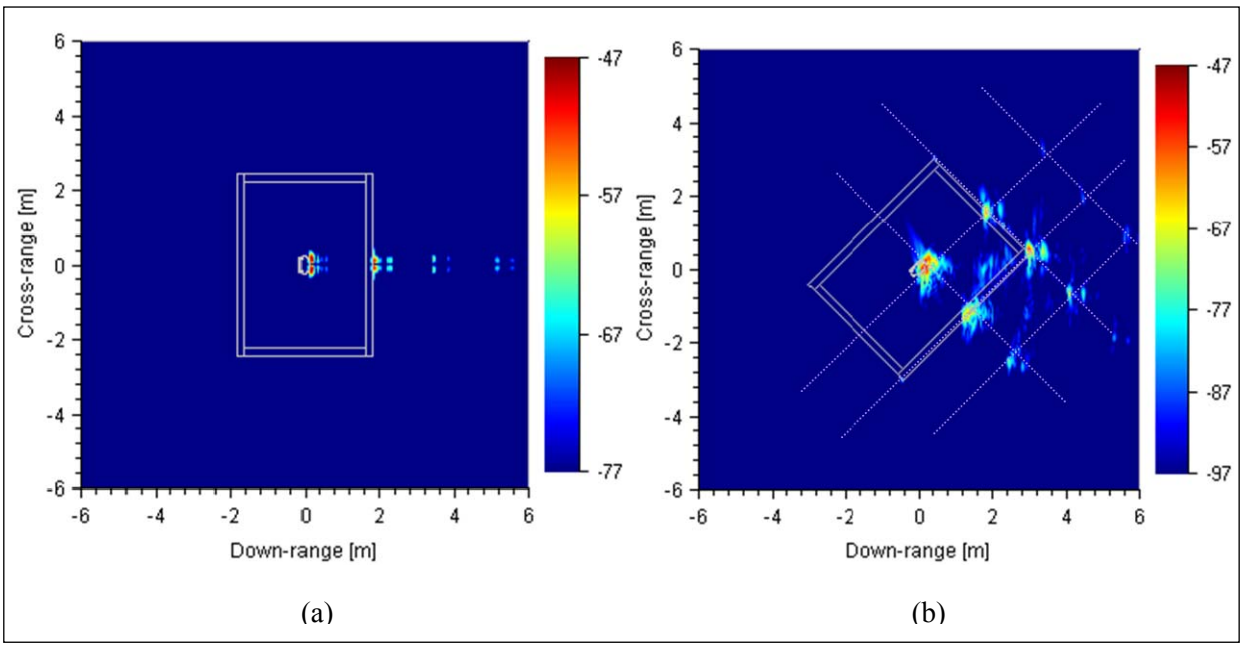

Figure A-3. SAR images of a simple room with brick walls in V-H polarization, showing multiple ghost images appearing at regular intervals behind the back wall(s): (a) broadside aperture and (b) 45° tilted aperture.

Note: The lower limit of the dB scale in figure A-3b was extended with 20 dB as compared to figure 23b.

In conclusion, we can state that a localized target in a room always produces at least one ghost image along a back wall (in reality, these images are slightly displaced outside the walls because of the wall propagation delays). This phenomenon was evident in the images in figure 9 obtained at oblique incidence. However, the human ghost image appears in the SAR images in figure 7 (broadside incidence) as well, this time as a shadow cast on the back wall image. In this case, the fields diffracted by the human and reflected from the back wall are in opposite phase with the fields reflected directly from the back wall; hence, their contributions subtract and we notice a "gap" in the back wall image, corresponding to the projection of the human.

List of Symbols, Abbreviations, and Acronyms

2-D	two-dimensional
ARL	U.S. Army Research Laboratory
BPA	backprojection algorithm
CAD	computer-aided design
CEM	computational electromagnetics
CERDEC	Communications-Electronics Research Development and Engineering Center
CPU	central processing unit
DoD	Department of Defense
EM	electromagnetic
FDTD	Finite Difference Time Domain
FFT	fast Fourier transform
H-H	horizontal-horizontal
I2WD	Intelligence and Information Warfare Directorate
MSRC	Major Shared Resource Center
MTI	moving target indicator
PDF	probability distribution function
PEC	perfect electric conductor
PFA	polar format algorithm
PO	physical optics
PRF	pulse repetition frequency
RF	radio frequency
SAIC	Science Application International Corporation
SAR	synthetic aperture radar
SIRE	Synchronous Impulse Reconstruction radar

STTW	sensing through the wall
UHF	ultra high frequency
UWB	ultra-wideband
V-H	vertical-horizontal
VHF	very high frequency
V-V	vertical-vertical

No. of Copies	Organization
1 ELEC	ADMNSTR DEFNS TECHL INFO CTR ATTN DTIC OCP 8725 JOHN J KINGMAN RD STE 0944 FT BELVOIR VA 22060-6218
1 CD	OFC OF THE SECY OF DEFNS ATTN ODDRE (R&AT) THE PENTAGON WASHINGTON DC 20301-3080
1	US ARMY RSRCH DEV AND ENGRG CMND ARMAMENT RSRCH DEV & ENGRG CTR ARMAMENT ENGRG & TECHNLGY CTR ATTN AMSRD AAR AEF T J MATTS BLDG 305 ABERDEEN PROVING GROUND MD 21005-5001
2	US ARMY RDECOM CERDEC INTELLIGENCE & INFO WARFARE DIRECTORATE (I2WD) ATTN AMSRD CER IW IM W CHIN ATTN AMSRD CER IW IM M FARWELL BLDG 600, MCAFEE CENTER FT MONMOUTH NJ 07703
1	PM TIMS, PROFILER (MMS-P) AN/TMQ-52 ATTN B GRIFFIES BUILDING 563 FT MONMOUTH NJ 07703
1	US ARMY INFO SYS ENGRG CMND ATTN AMSEL IE TD A RIVERA FT HUACHUCA AZ 85613-5300
1	COMMANDER US ARMY RDECOM ATTN AMSRD AMR W C MCCORKLE 5400 FOWLER RD REDSTONE ARSENAL AL 35898-5000
1	US GOVERNMENT PRINT OFF DEPOSITORY RECEIVING SECTION ATTN MAIL STOP IDAD J TATE 732 NORTH CAPITOL ST NW WASHINGTON DC 20402

No. of Copies	Organization
1	US ARMY RSRCH LAB ATTN RDRL CIM G T LANDFRIED BLDG 4600 ABERDEEN PROVING GROUND MD 21005-5066
15	US ARMY RSRCH LAB ATTN RDRL D OFFICE OF DIRECTOR ATTN IMNE ALC HRR MAIL & RECORDS MGMT ATTN RDRL CIM L TECHL LIB ATTN RDRL CIM P TECHL PUB ATTN RDRL SER M W O COBURN ATTN RDRL SER U A MARTONE ATTN RDRL SER U A SULLIVAN ATTN RDRL SER U C LE ATTN RDRL SER U K KAPPRA ATTN RDRL SER U K RANNEY ATTN RDRL SER U L NGUYEN ATTN RDRL SER U M RESSLER ATTN RDRL SER U D LIAO ATTN RDRL SER U T DOGARU (2 HCS) ADELPHI MD 20783-1197

TOTAL: 25 (1 ELEC, 1 CD, 23 HCS)

INTENTIONALLY LEFT BLANK.